Electrochimica Acta 404 (2022) 139726

Contents lists available at ScienceDirect

Electrochimica Acta

journal homepage: www.elsevier.com/locate/electacta

Physics-based modeling of sodium-ion batteries part I: Experimental parameter determination

Kudakwashe Chayambuka[a,b,c], Ming Jiang[a,d], Grietus Mulder[a,b], Dmitri L. Danilov[a,d], Peter H.L. Notten[a,d,e,*]

[a] Eindhoven University of Technology, Postbus 513, 5600MB Eindhoven, Netherlands
[b] VITO, Boeretang 200, 2400 Mol, Belgium
[c] EnergyVille, Thor Park 8310, 3600 Genk, Belgium
[d] Forschungszentrum Jülich, Fundamental Electrochemistry (IEK-9), D-52425 Jülich, Germany
[e] University of Technology Sydney, Broadway, Sydney, NSW 2007, Australia

ARTICLE INFO

Article history:
Received 14 July 2021
Revised 7 December 2021
Accepted 7 December 2021
Available online 9 December 2021

Keywords:
Sodium-ion batteries
Sodium-ion battery modeling
Electrochemical parameters
P2D battery parameters
Hard carbon
NVPF

ABSTRACT

Sodium-ion batteries (SIBs) have been heralded as the most promising “beyond lithium” energy storage technology. This proclamation is based on recent technological trends and the outstanding performance of the state-of-the-art prototype 18650 and pouch cells. However, improving the design and performance of SIBs requires an in-depth understanding of the electrochemical behavior of the electrodes from both an experimental and physics-based modeling perspective. In this contribution, experimental characterizations of SIB electrode materials based on $Na_3V_2(PO_4)_2F_3$ (NVPF) cathode and hard carbon (HC) anode are presented. The goal of this experimental investigation is to understand the individual electrode behavior and further elucidate relevant parameters for physics-based models. As a result, geometric, thermodynamic, and kinetic parameters are deduced from the two SIB electrodes. Based on the analyses of Na//NVPF and Na//HC half-cells, diffusion mass transport limitations and Ohmic losses are identified for both electrodes. These overpotential losses are equally present in full cell SIBs composed of NVPF and HC electrodes. These results are useful in the setup of SIB physics-based models.

1. Introduction

Sodium-ion batteries (SIBs) are an emerging class of rechargeable batteries, which have been proclaimed as the most viable complementary technology to the ubiquitous lithium-ion batteries (LIBs) [1–3]. Although both LIBs and SIBs were discovered around the same time in the 1970s, interests in SIBs quickly faded soon after, due to the failure of Na intercalation in graphite and the lack of alternative anode materials [4]. The rejuvenated interest in SIBs can be traced to the discovery of hard carbon (HC) as SIB anode by Stevens and Dahn in the year 2000 [5,6]. Since then, unprecedented progress has been witnessed in the SIB technology, predominantly in the last decade [7]. This is evidenced by several milestone achievements such as the discoveries of new classes of cathode materials and the assembly of full cell SIBs [8,9]. In addition, commercialization efforts also began in the last decade, and have been spearheaded by start-ups such as Faradion, Tiamat, Altris, and HiNa [10–15]. The main driver for this technological trend is the supply shortage risk of LIB materials [1]. Therefore, the availability of several nickel- and cobalt-free chemistries is expected to result in sustainable, low-cost and high energy dense SIBs.

Among the several possible combinations of SIB active materials, one of the most promising is the one based on the $Na_3V_2(PO_4)_2F_3$ (NVPF) cathode and HC anode [13]. This battery was first developed via the collaboration of the French National Center for Scientific Research (CNRS), Alternative Energies and Atomic Energy Commission (CEA), and the Collège de France, under the umbrella of the French network for electrochemical energy storage (RS2E) [10]. These efforts culminated in the first cylindrical 18,650 SIBs in 2015 [10]. In other investigations, the electrolyte composed of $NaPF_6$ salt and equal weight mixtures of ethylene carbonate (EC) and propylene carbonate (PC) was identified as a stable electrolyte composition in SIB systems [16]. It is therefore judicious, to further investigate this combination of electroactive compounds, in order to understand the characteristics of the HC//NVPF SIB.

---

[*] Corresponding author.
E-mail address: p.h.l.notten@tue.nl (P.H.L. Notten).

https://doi.org/10.1016/j.electacta.2021.139726
0013-4686/

NVPF and HC are two electrode materials with different structures and charge storage mechanisms. NVPF belongs to the NASICON (Natrium Superionic Conductor) family of compounds [17–19]. Charge insertion in NVPF occurs via the reversible intercalation mechanism [20,21]. Because of the multiple oxidation states of vanadium, *i.e.* V^{3+}, V^{4+}, and V^{5+} and the inductive effects of the $(PO_4)^{3-}$ and F^- anions, NVPF exhibits a high cathodic voltage [22–24]. The charge transfer process in NVPF can be written as

$$Na_3V_2^{III}(PO_4)_2F_3 \rightleftharpoons NaV_2^{IV}(PO_4)_2F_3 + 2Na^+ + 2e^-. \quad (1)$$

Eq. (1) is a general electrochemical half-reaction showing the reversible exchange of 2 Na^+ per formula unit in NVPF. This results in a theoretical capacity of 128 mAh g^{-1}, which makes NVPF one of the most stable and high energy dense SIB cathode materials [2].

On the other hand, the HC anode is structurally composed of graphene-like parallel layers embedded in a microporous amorphous phase [5]. Charge insertion in HC occurs via mechanisms of mesopore/nanopore filling and adsorption on graphene layers [25–27]. It should be mentioned that correlating the microstructural properties of HC to the observed voltage profiles remains controversial and an active area of research [2,28]. Nevertheless, HC achieves an impressively high specific capacity of about 300 mAh g^{-1} which approximates to that of graphite in LIBs.

In this work, the experimental methods applied to both NVPF and HC electrodes are described, in order to derive parameters for physics-based, pseudo-two-dimensional (P2D) modeling. The P2D equations and model structure are described elsewhere [29]. These models generally require many parameters, which are classified as geometric, thermodynamic, transport, and kinetic properties [30,31]. As many as 35 model parameters were recently identified [32]. For a new battery chemistry, such as the SIB, the need for reliable, experimentally determined parameters cannot be overstated. This problem is further complicated by the fact that most parameters are either unknown or not agreed upon. Yet, these model inputs within reasonable accuracy constitute the backbone for accurate, physics-based models. It is therefore imperative that the battery modeling parameters be derived from dedicated experiments designed for this purpose.

The physical and electrochemical parameters of room temperature SIBs based on NVPF and HC electrodes and 1 M $NaPF_6$ $EC_{0.5} : PC_{0.5}$ (w/w) electrolyte are herein determined using half-cell and full cell experimental setups. The experiments are specifically designed for parameter determination and P2D model validation. Physical property tests based on Scanning Electron Microscopy (SEM), electrochemical tests based on three-electrode half-cell gravimetric intermittent titration technique (GITT) tests, and three-electrode full cell (dis)charge rate tests are used as a strategy to yield 15 model parameters in a few dedicated investigations. From the GITT analyses, concentration-dependent kinetic rate parameters and diffusion coefficients can be further derived [33]. Because battery manufacturers do not typically provide the requisite extensive parameter set, these experimental characterizations are necessary complementary tools to enable accurate P2D modeling.

2. Experimental

A PAT-Cell (EL-Cell GmbH, Hamburg, Germany) was used as the electrochemical test cell. The PAT-Cell is composed of an 18 mm diameter PAT-core in which battery electrodes can be assembled. The PAT-core components include a factory-assembled separator surrounded by a prefabricated Na-metal ring, which acts as the reference electrode (Na-RE). This configuration allows the Na-RE to be close enough to the battery electrodes for accurate measurements. In addition, two stainless steel upper and lower plungers complete the PAT-core configuration, allowing external electrical contact and uniform pressure distribution on the electrodes. In configuring the PAT-core, it is also important to select the correct lower plunger size, which ensures good electrode contact with the separator and avoids electrolyte leakage. Detailed images of the EL-Cell PAT-cell are shown in Fig. 1.

Half-cells and full cells were thus assembled in an argon-filled glove box (Innovative Technology, Inc. Newburyport, MA), where oxygen and moisture levels were controlled below 1 ppm. These conditions prevent surface oxidation of the highly reactive metallic sodium electrodes. After assembly, the PAT-Cells were hermetically sealed with a polyethylene sealing ring and placed in a climate chamber (Maccor, model MTC-010) at 25 °C. Cell voltage measurements were recorded using Maccor® automated cycling equipment (Model 4200), and cycling programs were configured in Maccor® standard test software (MacTest 32).

Reproducible results were obtained with the PAT cells. Furthermore, the Na-RE was stable at all test conditions. The half-cell configuration allows individual electrodes to be cycled to their full capacity. As metallic Na counter electrodes (CE) were used, it is necessary to use thick separators, which can withstand dendrite growth. Na-RE in a three-electrode configuration was used to obtain accurate measurements of the working electrode potentials. Such a design eliminates additional overpotentials arising from the thick separator and metallic CE.

2.1. Electrodes

Dry, double-side coated NVPF and HC electrodes with single-side mass loadings of 12 and 6 mg cm^{-2} respectively, were used. These coated electrodes were supplied by the manufacturer (SAFT/CEA). The electrode balancing work was completed in the recently concluded in the EU-funded NAIADES project [34,35]. Because sodium does not alloy with aluminum at the anode-side, aluminum was used as the current collector for both electrodes. The advantages of using aluminum instead of copper as the anodic current collector have been discussed recently [1]. The double-coated electrodes were first scrapped on one side to delaminate and expose the current collector using a surgical blade. It is advisable to delaminate only the small area intended to be cut out because single-side coated electrodes curl and become difficult to handle. 18 mm diameter electrodes were then cut to size using an 18 mm diameter electrode punching tool. Better cuts were obtained when the laminated side was cut facing up on a soft plastic base. This procedure was followed for both the NVPF and HC electrodes.

Unlike lithium, which is commercially available as a foil, sodium is sold in cubes immersed in mineral oil. To prepare thin sodium electrodes, sodium metal cubes (Aldrich, 99.9%) were first washed with propylene carbonate to remove the mineral oil and then wiped dry with a soft tissue. The cube was then cut in half using a surgical blade to expose the pristine metal surface. The half-cube and aluminum foil were then sealed in a polypropylene plastic bag. This procedure was carried out inside the glove box.

To prepare flat sodium electrodes, the sealed bag was taken outside the glove box, and the cube was pressed against the aluminum foil using a hydraulic press until a flat electrode surface was obtained. The plastic protects the pristine metal surface from the air contamination and sticking to the press. The aluminum foil, therefore, becomes the current collector. Sodium electrodes with a thickness of 400 µm were thus obtained. After pressing, the sealed sodium electrode was reintroduced in the glove box, and 18 mm diameter electrodes cut to size using the electrode punching tool. Other studies have established that the procedure for making sodium electrodes has a significant impact on the stability of electrochemical results [36–38]. This is consistent with our

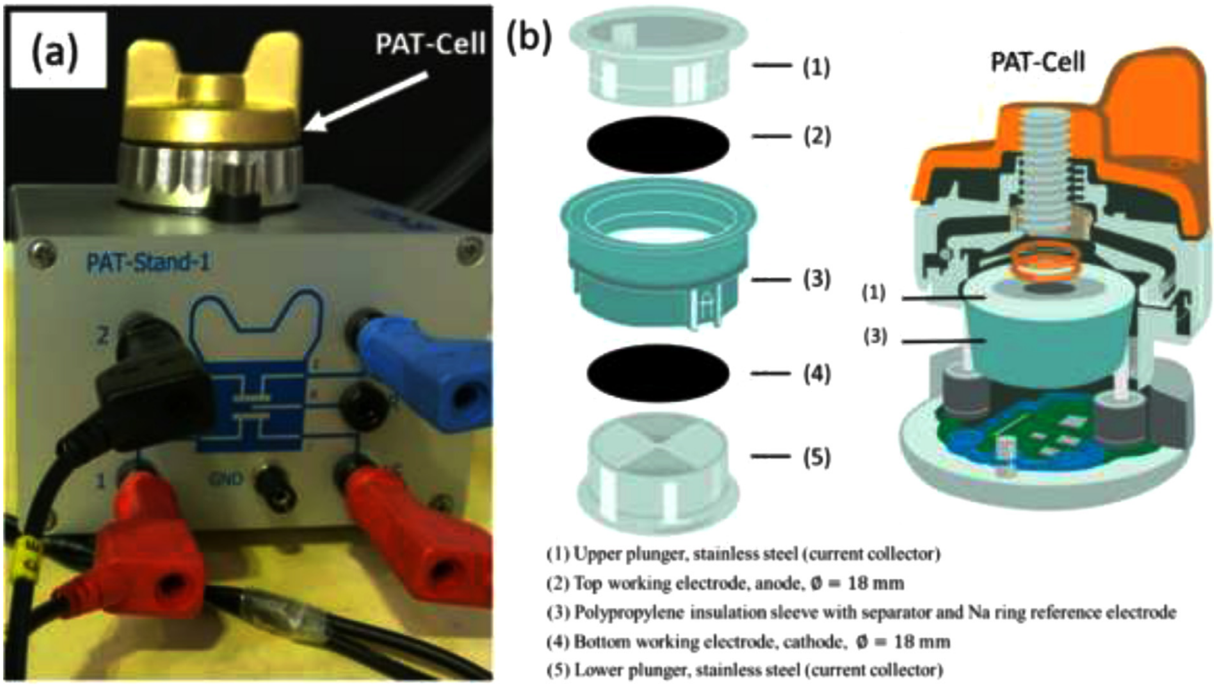

Fig. 1. The PAT-Cell components and configuration. Image of the PAT-Cell inside a climate chamber showing the potentiostat cable connectors and PAT-Stand which enables the connection with the PAT-Cell to the potentiostat cables (a). Components of the PAT-Cell (b).

own findings. The sodium electrodes obtained after pressing are shown in the Supplementary Information (Fig. S1).

2.2. Electrolyte

1 M $NaPF_6$ $EC_{0.5} : PC_{0.5}$ (w/w) electrolyte was prepared starting with pure solvents and salt. Equal mass samples of EC and PC were mixed before being heated and stirred at 60 °C. The heating allows EC to melt and dissolve. The salt, $NaPF_6$ (Kishida, anhydrous, 99.0%) was finally dissolved in the $EC_{0.5} : PC_{0.5}$ (w/w) solvent to make an electrolyte of 1 M concentration, which was used in all investigations. This procedure was carried out in the glove box. No electrolyte additives were used, and all electrolytes and salts were used as received.

2.3. Physical property analyses

Scanning electron microscopy (SEM) micrographs obtained on Quanta FEG 650 (FEI, USA) environmental SEM operated at a voltage of 20 kV were used to analyze the morphology of the NVPF and HC electrodes as well as the 25 µm FS 3005–25 separator (Freudenberg Viledon). Gold sputtering was applied to the samples to enhance conductivity and reduce charge accumulation during measurements. The particle size distribution and the average particle radii of the positive and negative electrodes were determined from the scan images.

The thicknesses of the double-side coated NVPF and HC electrodes, and the aluminum current collectors were measured by a digital-micrometer screw gage (Helios Preisser, Digi-Met). Thickness measurements were taken at random points of the electrodes. The average, single-side coating thickness was obtained by subtracting the current collector thickness from the average double-side coating thickness and dividing by 2. Electrode porosity was provided by the manufacturer (SAFT/CEA), while the thickness and porosity values of the separator were taken from the corresponding datasheets [39].

2.4. Electrochemical testing

The voltage profiles of the NVPF and HC electrodes were determined by three-electrode, half-cell measurements. These cells were composed of the aforementioned Na metal electrode as CE, a prefabricated Na-RE, and either a NVPF or HC porous electrode as working electrodes. In addition, 1 M $NaPF_6$ electrolyte and a 220 µm thick FS-5P separator (Freudenberg Viledon FS 2226E + Lydall Solupor 5P09B) were used. The FS-5P separator is composed of two layers of nonwoven polypropylene fiber (FS: 180 µm thick, 67% porous) and a microporous polyethylene film (5P: 38 µm thick, 86% porous). Because of this composition and thickness, the FS-5P separator has a high porosity, good wettability, and high resistance to dendrite growth. These characteristics make it a good choice for half-cell tests.

After assembly in the argon-filled glove box, the PAT-Cell was hermetically sealed and placed in a climate chamber at 25 °C. The Na//NVPF half-cells underwent 5 formation cycles at a constant current of 0.1 mA / 0.039 mA cm^{-2} (corresponding to approximately C/30, where C-rate is based on the storage capacity obtained at slow (dis)charge rate) in the cell voltage range of 3.0 to 4.3 V *vs.* Na^+/Na. The formation stage allows the growth of a protective surface layer on the active electrode particles and results in stable cycles [40]. After the formation stage, the cells were charged in 3 consecutive stages: (i) 0.1 mA constant current (CC) charging until the upper cutoff cell voltage of 4.3 V, (ii) constant voltage (CV) charging for 3 h at 4.3 V, and (iii) open-circuit voltage (OCV) relaxation for 1 hour. The CV stage allows the maximum cell capacity to be reached, while the OCV period allows the sodium concentration gradients to equilibrate. After charging, the cell underwent discharge rate testing at different currents of 0.1, 0.2, 0.3, and 0.4 mA, corresponding to C/30, C/15, C/10, and C/7.5, respectively. After each discharge rate test, the above-mentioned 3 stage charging protocol was repeated to maintain consistency in the initial discharging starting point.

The Na//HC half-cells similarly underwent an identical formation and cycling procedure in the voltage range of 0.3 mV to 2.0 V *vs.* Na^+/Na. The formation stage consisted of 5 CC (dis)charge cycles at 0.2 mA / 0.078 mA cm^{-2}, corresponding to approximately C/15. After formation, a 3-stage discharge protocol was applied comprising of: (i) 0.1 mA CC until a cutoff voltage of 2 V has been reached (ii) 3 h CV at 2 V followed by (iii) a 1-hour OCV relaxation period. Discharge herein refers to Na extraction from the HC electrodes, which increases the electrode potential. The half-cells were then sodiated upon charging at different rates of 0.1, 0.12, 0.14, and 0.16 mA (C/30, C/25, C/21, and C/19) until the cutoff voltage of 0.3 mV. Because of a long and flat voltage plateau close to 0 V *vs.* Na^+/Na, finding the optimal lower cutoff voltage for the HC electrode is indeed challenging [36,41]. This is because during charging, it is important to maintain HC electrode potentials above zero volts, to avoid Na plating and dendrite formation. However, the cutoff potentials are defined by the total cell voltage, a value which contains contributions of all overpotentials, including the activation and charge transfer overpotential of the CE electrode and the electrolyte Ohmic drop. For the HC electrode, a cell cutoff voltage of 0.3 mV, however, resulted in a high electrode capacity without Na plating. This cutoff voltage value can be different in other setups.

2.5. Determination of electrode parameters using GITT

Galvanostatic intermittent titration technique (GITT) was performed with the assembled Na//NVPF and Na//HC half-cells. Starting with a fully discharged Na//NVPF half-cell, 30 GITT steps were applied, which comprised of a CC charging pulse of 0.1 mA (C/30) until the cell capacity reached 0.1 mAh followed by an OCV rest period of 1 hour. Because Coulomb counting was used to define the pulse duration (and not time), each GITT pulse was approximately 1 hour long. A low current of C/30 was applied during the CC period, in order to minimize voltage overpotentials. The OCV stage was set for a duration of 1 hour, a time in which voltage relaxation is expected to reach a steady-state. After the 30 GITT steps, the cells were then fully charged to 4.3 V in CV mode for 5 h.

GITT with the assembled Na//NVPF half-cells was similarly performed using discharge current pulses. Starting with the fully charged cells, 30 GITT steps were applied, which comprised of a CC discharge pulse of 0.1 mA (C/30) until the discharge capacity reached 0.1 mAh, followed by an OCV relaxation period of 1 hour. After the 30 GITT steps, the cells were then finally discharged to 3 V in the CV mode for 5 h.

The GITT procedure with the assembled Na//HC half-cells was performed using discharge current pulses. The cells were initially charged using a CC of 0.1 mA (C/30) until the cell voltage reached 0.3 mV. This cutoff voltage corresponds to fully charged HC electrodes. Afterward, 29 GITT steps were applied to the cells, which comprised of CC discharge at 0.1 mA until the capacity reached 0.1 mAh followed by OCV relaxation for 1 hour. The Na//HC half-cells were then finally were discharged at a CV of 2 V for a period of 5 h. Because of the challenges at low anode potentials, namely the risk of Na plating and the flat low voltage profile of the HC electrodes, the GITT procedure could only be performed with discharge current pulses.

2.6. Full cell cycling

Galvanostatic discharge cycles of the HC//NVPF full cells were performed in a three-electrode setup, which included a Na-RE. The anode and cathode were comprised of 18 mm diameter, single-side coated NVPF and HC electrodes, respectively. In addition, a 25 µm FS 3005–25 separator and 1 M $NaPF_6$ $EC_{0.5}:PC_{0.5}$ (w/w) electrolyte were used. Unlike in the half-cell configurations, wherein thick, 220 µm separators had to be used, thin 25 µm separator were used in the full cells. This is because there is less risk of short circuits as a result of dendrite formation in full cells. Furthermore, a thin separator resembles the thickness used in practical SIBs. Therefore, the full cell setups closely mimic the performance of real SIBs.

After assembly in the argon-filled glove box, the PAT-Cell was hermetically sealed and placed in a climate chamber at 25 °C. 5 formation cycles at 0.2 mA were applied to the cells in the voltage range of 2.0 to 4.2 V. This allowed a solid electrolyte interface (SEI) formation and stabilization of the cell capacity. After formation, the cells underwent multiple discharge cycles at different current densities of 0.5, 1, 2.5, 5, 7.5, 10, 12 and 24 A m^{-2}, corresponding to 0.05, 0.1, 0.3, 0.6, 0.9, 1.2, 1.4 and 3 C, respectively, where 1C-rate = 8.3 A m^{-2}. To maintain consistency in the starting point of discharging, the charging cycle was performed in three stages: (i) galvanostatic CC charging at 0.2 mA, until the cell voltage of 4.2 V (ii) potentiostatic CV charging at 4.2 V for 3 h and (iii) OCV relaxation for 1 hour. This 3-stage charging procedure is designed to maintain constant initial concentrations without concentration gradients in either the electrode particles or the electrolyte. This charging procedure results in initial conditions consistent with the initial value considerations in the P2D model.

3. Results and discussion

In the nomenclature of variables, a distinction is made between electrode and electrolyte parameters. In addition, an effort is herein made to distinguish between positive (NVPF) and negative (HC) electrode parameters. For instance, the concentration, diffusion coefficient, and kinetic rate parameters are written in the form: $c_{\theta,m}$, $D_{\theta,m}$ and k_m, respectively. The subscript θ symbolizes the phase of the variable, which can either be in the solid phase ($\theta = 1$) or in liquid/electrolyte phase ($\theta = 2$) and the subscript m symbolizes the cell domain, which can either be the positive NVPF electrode ($m = p$), the negative HC electrode ($m = n$) or the separator ($m = s$).

3.1. Physical analyses

Fig. 2 shows SEM micrographs of the NVPF and HC electrodes at different magnifications. The NVPF and HC active particles have a diameter of the order of 1 µm and 10 µm, respectively. A mesoporous phase of conductive additives and binders can similarly be observed at a sub-micron scale. The NVPF particles have in general smooth, spherical shapes, while the HC particles have irregular cubic shapes with sharp edges. The edges on the HC particles constitute highly reactive sites for electrochemical reactions [42]. The NVPF electrode exhibits a dual-scale porosity in its microstructure due to the agglomeration of active particles. Similar agglomerates have also been identified in $LiNi_{0.5}Co_{0.2}Mn_{0.3}$ electrodes [43]. Outside these agglomerates, macropores with a diameter of approximately 3 µm can be identified in the NVPF electrode at a magnification of 13.000. This dual-scale porosity is known to improve the overall rate performance of the electrodes [44]. This is because the macropores result in electrodes with low tortuosity and act as transport “highways” for Na^+ ions in the electrolyte.

Fig. 3a and b show the particle size distribution of NVPF and HC electrodes. The average active particle radii of NVPF and HC are 0.59 and 3.48 µm, respectively. The two electrodes, however, exhibit a wide dispersion of particle sizes. The distribution of HC electrode particles, in particular, has a high standard deviation of 2.5 µm. In contrast, the NVPF electrode shows a standard deviation of 0.5 µm. The irregular shapes and the large particle size distribution in the HC electrode increase the slurry viscosity, which has been reported as one of the challenges encountered during HC electrode coating at industrial scale [2,45–47].

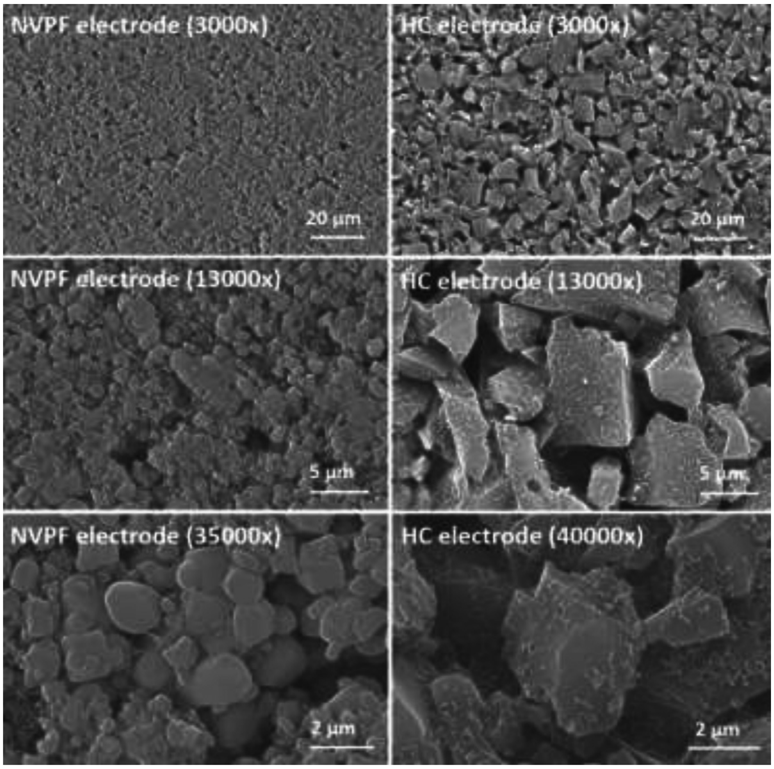

Fig. 2. Top view SEM micrographs of NVPF and HC electrodes at different magnifications.

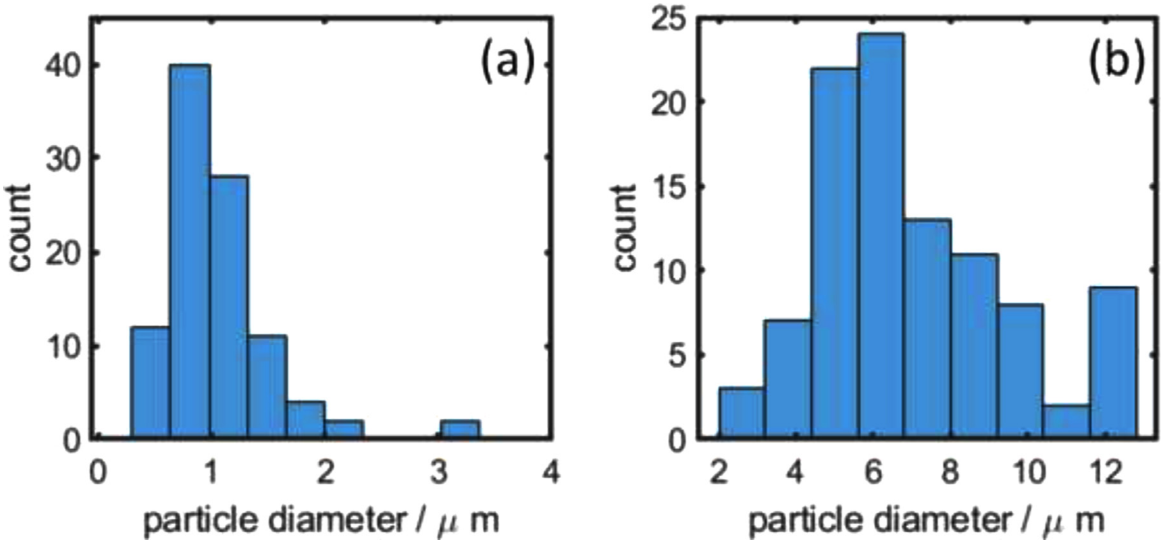

Fig. 3. Electrode particle size distribution of NVPF (a) and HC (b). Particle sizes determined from SEM micrographs.

Fig. 4a and b show SEM images of the FS 3005–25 separator used in the full cell SIBs. This separator is composed of a polypropylene fiber base impregnated by a mixture of binder and Al_2O_3 ceramic particles. The fibers and the particles can be observed at both magnifications. Fig. 4c shows the cross-section image of a double-side coated NVPF and HC electrode with a separator in between. On each electrode, 3 layers representing the Al current collector (in the middle) and two porous electrode coatings on either side of the Al current collector can be observed. It can also be observed that the NVPF electrode is more compact and hence has less porosity than the HC electrode. The average thickness of the Al current collector is 22 µm while the average thickness of double-side coated NVPF, and HC electrodes including the current collector are 158 and 149 µm, respectively.

Table 1 summarizes the physical electrode properties obtained. These electrode dimensions constitute important inputs in P2D models because the optimization of the electrode thickness and particle size, starting with unknown parameters, requires remeshing and changes to the model time step, which can cause model instability. Moreover, the determination of extended parameters such as diffusion coefficients and kinetic rate constants is dependent on the accurate knowledge of the particle size and electrode thickness measurements. For these reasons, it is important to carry out extensive physical property characterizations of battery elec-

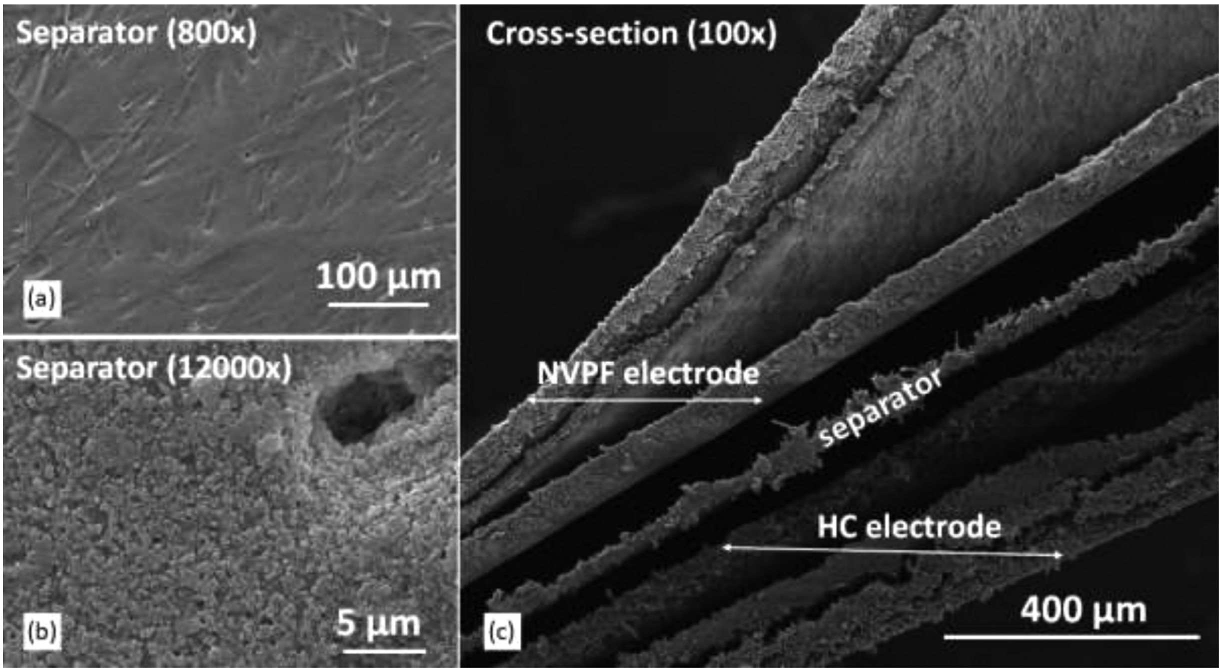

Fig. 4. SEM micrographs of a FS 3005–25 separator at a magnification of 800 (a) and 12.000 (b). Cross-sectional view of double-side coated NVPF electrode, HC electrode, and FS 3005–25 separator (c).

Table 1
Summary of physical properties of the main SIB components.

Parameter	Unit	Description	NVPF	HC	Separator
L_{double}	µm	Double-side coating thickness (average)	153-163 (158)	137-155 (149)	-
L_{CC}	µm	Current collector thickness	22	22	-
δ_m	µm	Single-side thickness	68	64	25
R_m	µm	Mean particle radius	0.59	3.48	-
ρ_m	g cm^{-3}	Density	3.2$^{(a)}$	1.6-2.0$^{(b)}$ (1.95)	1.4
A	cm^2	Area	2.545	2.545	2.545
ϵ_m^{el}	-	Electrolyte volume fraction	0.20-0.25	0.49-0.52	0.55

(a) data derived from Dugas et al. [40]
(b) data derived from available literature sources [40,48–50]

trodes. Nevertheless, holistically incorporating the material properties in P2D models is not straightforward either. This is because P2D models conceptually consider spherical, monodisperse particles whereas, in reality, electrodes can have a broad particle size distribution, and the particles can have a variety of shapes (as shown in Figs. 2 and 3). In most cases however, the particles can be assumed spherical, and the average particle size and electrode thickness can be used as the approximate and representative physical parameters.

3.2. Na//NVPF half-cell

Fig. 5 shows the results from 3-electrode electrochemical testing of a Na//NVPF half-cell in the voltage range of 3 to 4.3 V. The voltage profile of the NVPF electrode exhibits a characteristic steep voltage step around 3.7 to 4.1 V *vs.* Na$^+$/Na. Fig. 5a shows formation (dis)charge cycles performed at 0.1 mA (0.039 mA cm^{-2}, C/30). The electrode records a reversible capacity of 94, 98, and 103 mAh g^{-1} in the 1st, 2nd and 5th cycle, respectively. In the 1st cycle, voltage artifacts around 3.8 V are observed. Note, these 1st cycle artifacts are only recorded in Na//NVPF half-cells, and are related to secondary electrochemical reactions occurring at the Na CE [37]. Subsequent cycles, however, demonstrate voltage stability and improved Coulombic efficiency. Fig. 5b shows dQ/dV curves for the 2nd and 5th cycle. Despite an increase in electrode capacity in the 5th cycle, the derivatives look similar four voltage plateaus marked in Roman numerals I to IV can therefore be distinguished in the voltage range of 3.6 to 4.3 V *vs.* Na$^+$/Na. Such a step-wise voltage profile is associated with crystallographic phase transitions in the NVPF electrode material [51,52].

Fig. 5c shows the low current voltage discharge profiles of an NVPF electrode at 0.1, 0.2, 0.3, and 0.4 mA, corresponding to C/30, C/15, C/10, and C/7.5, respectively. The Roman numerals I to IV are again used to mark the respective voltage plateaus. Using the extrapolation-to-zero-current method, the equilibrium potential (EMF) can be determined from the voltage profiles at low rates. The as-obtained EMF is shown in Fig. 5c by the black line. Details of the extrapolation-to-zero-current method have been described by Danilov et al. [53–55]. Fig. S2 in the Supplementary Information shows more details about the determination of the NVPF EMF. Based on the NVPF EMF, a reversible electrode capacity of 101 mAh g^{-1} is determined. Fig. 5d shows the NVPF electrode overpotential and rate-dependent discharge capacity as a function of discharge current. Considering more or less linear dependencies, the NVPF storage capacity decreases with increasing current density at a rate of 28 h cm^2 g^{-1}, while the average overpotential increases at a rate of 370 Ω cm^2. The average overpotential is calculated from the voltage difference between the EMF and the various voltage discharge curves. These numbers are highly relevant for a

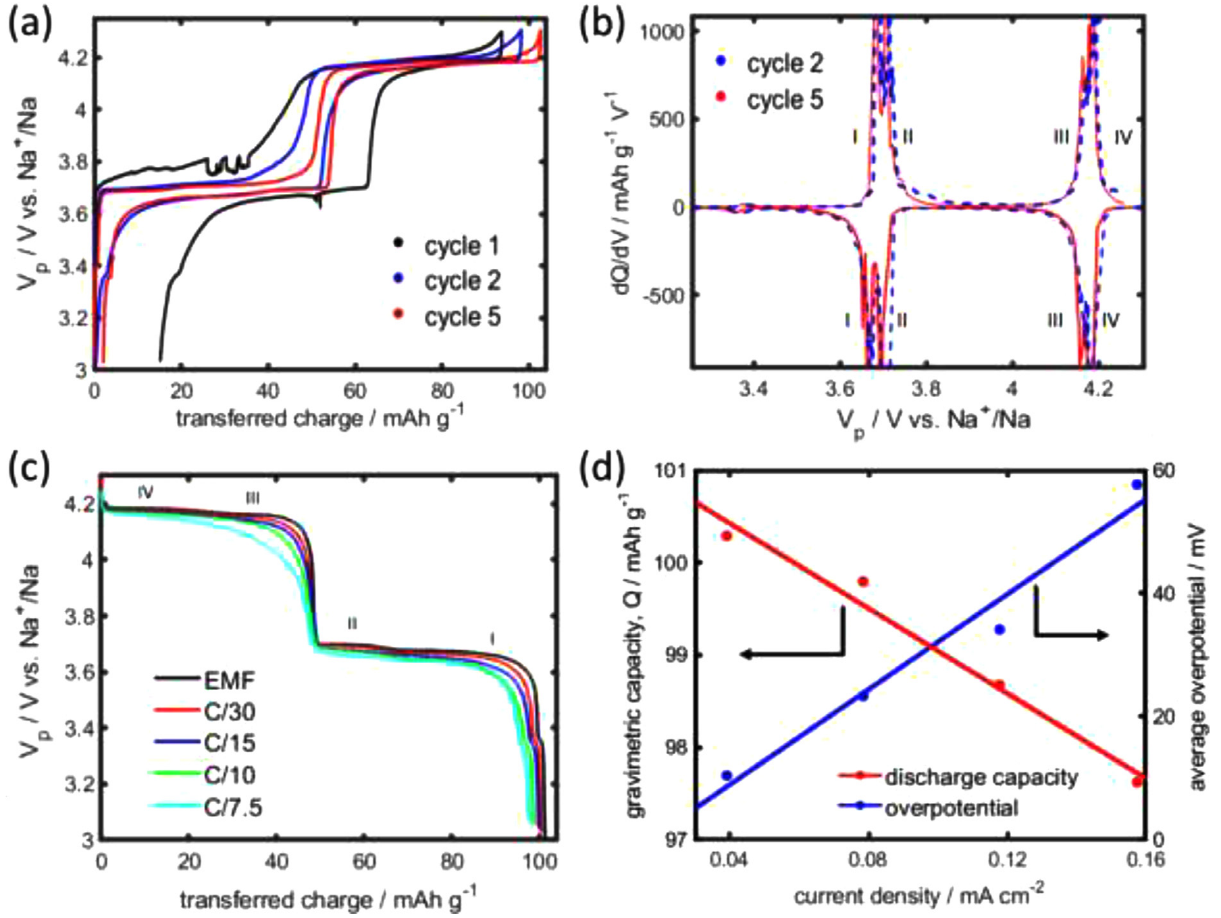

Fig. 5. Na//NVPF half-cell tests. Formation (dis)charge cycles, showing the electrode potential as a function of the transferred charge (a). dQ/dV curves of the 2nd and 5th cycle *vs.* the electrode potential (b). Low-current voltage discharge profiles of the NVPF electrode obtained at C/30, C/15, C/10, and C/7.5 (c). NVPF electrode rate-dependent discharge capacity (red line) and average overpotential (blue line) as a function of discharge current density (d).

comparison with those found for the HC electrode to be presented below.

3.3. Na//HC half-cell

Fig. 6a shows the (dis)charge formation cycles obtained with a HC electrode at 0.2 mA (C/15 rate). Using a cutoff cell voltage of 0.3 mV, the electrode has a first cycle capacity and irreversible capacity loss of 125 and 9 mAh g^{-1}, respectively. The first cycle irreversible capacity loss is defined as the difference between the charging and discharging capacities. This difference is caused by entrapped Na in the micropores [56]. The HC irreversible capacity loss of only 9 mAh g^{-1} is impressively low. By comparison, larger irreversible capacity losses of approximately 62 mAh g^{-1} have been reported before [40]. Because in a full cell configuration, the cathode is the only source of intercalated Na$^+$ and the standard practice is to oversize the anode to avoid Na plating, any irreversible capacity related to the anode is therefore highly detrimental to the storage capacity [56]. The relatively low irreversible capacities of HC found herein is therefore very favorable for assembling high capacity SIBs.

The subsequent HC cycles in Fig. 6a show improved Coulombic efficiencies. For example, the irreversible capacity loss found in the 5th cycle reduces to only 1 mAh g^{-1}. However, the HC electrode shows a significant voltage difference between (dis)charge cycles. Because this has an effect of reducing the energy efficiency of full cells, this phenomenon will be discussed in relation to full cell SIB voltage profiles.

Fig. 6b shows the dV/dQ curves of the HC electrode in the 1st and 5th cycles. Identical dV/dQ profiles for the two cycles demonstrate a highly stable cycling behavior. The charge and discharge plateaus are located at 0.06 and 0.12 V *vs.* Na$^+$/Na, respectively. An SEI peak located at 0.9 V, as previously reported by Dugas *et al.* [40], is however not so pronounced in the present study due to the fact that no electrolyte additives were used.

Fig. 6c shows the voltage curves of an HC electrode during charging at 0.1, 0.12, 0.14, and 0.16 mA (C/30, C/25, C/21, C/19). Again, using the extrapolation-to-zero-current method [53–55], the EMF of the HC electrode has been determined. Fig. S3 shows the details of this determination for the HC EMF. Based on the EMF, a reversible electrode capacity of 222 mAh g^{-1} is obtained (black curve in Fig. 6c). At the low charging current of 0.1 mA (C/30), the HC electrode has a capacity of 187 mAh g^{-1}. Increasing the charging rate from 0.1 mA to 0.16 mA results in a 23% decline in electrode capacity, *i.e.* from 187 to 144 mAh g^{-1}. Such a rapid decline demonstrates the difficulty to access the full capacity of the HC electrode because of the flat, low-voltage plateau toward full charge. It also points to a potential challenge for fast charging HC-based SIBs; because of the very low rates required to reach the full capacity while avoiding Na plating on the anode.

Fig. 6d shows the variation of the electrode capacity and average overpotential as a function of current density. The average overpotentials at different charge rates are calculated as the average voltage difference between the HC EMF and the HC voltage profile at a given charge rate. As the current density increases, the rate-dependent electrode capacity linearly decreases at a rate of

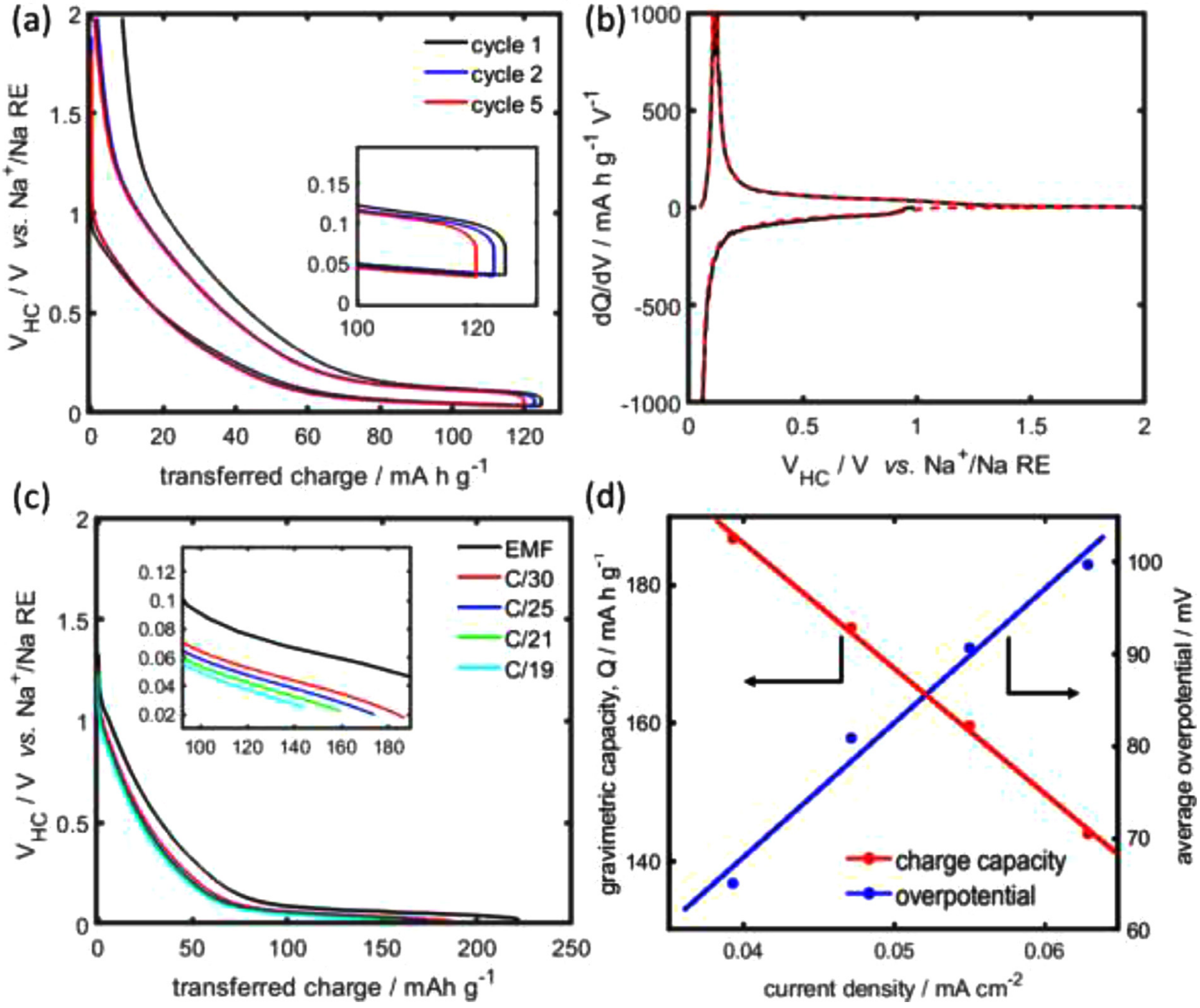

Fig. 6. Formation (dis)charge cycles of a Na//HC half-cell, showing the electrode potential *vs.* transferred charge (a). dQ/dV curves of the 1st and 5th cycles *vs.* electrode potential (b). Low current voltage charge curves at C/30, C/25, C/21, and C/19 (c). HC charge capacity (red line) and overpotentials (blue line) at the different discharge rates (d).

1780 h cm^2 g^{-1}, while the overpotential increases linearly at a rate of 1600 Ω cm^2. Both numbers are significantly higher in comparison to those of the NVPF electrode (Fig. 5d), indicating that the HC electrode can be considered as the rate-limiting and capacity-limiting electrode in charging SIBs.

3.4. GITT measurements

Fig. 7 shows an overview of the 30 GITT steps obtained for the NVPF electrode in the voltage range of 3.0 to 4.3 V during charging (a) and discharging (b). The CC pulses are shown in red symbols while the OCV rest periods are shown in blue. Fig. 7 also shows in more detail, the cathode voltage profiles, in the voltage range of 3.6 to 3.7 V *vs.* Na$^+$/Na during charging (c) and discharging (d). At this higher magnification, 2 Vage plateaus separated by about 20 mV can be identified, which were hardly visible in Fig. 7a and b. The voltage plateaus correspond to phase transition regions, while the voltage slopes correspond to solid solution regions [57]. Fig. 7 further shows in more detail, the GITT profiles in the upper-voltage plateau region, in the voltage range of 4.1 to 4.2 V *vs.* Na$^+$/Na during charging (e) and discharging (f). Voltage plateaus can also be identified in this voltage region, although the separation of the plateaus is not as distinct as in the low voltage region. In Fig. 7c to f, variations in the GITT relaxation periods can be discerned at voltage slopes and voltage plateaus. These changes can be attributed to changes in the diffusion coefficient and phase transition in the material [58].

Fig. 8a shows the 29 GITT steps obtained for the HC electrode during discharging in the voltage range of 0.3 mV to 2.0 V. The CC pulse and OCV relaxation are shown in red and blue dots respectively. Fig. 8 also shows in more detail, the GITT profiles in the voltage sloping region (b) and in the low voltage plateau region (c). Compared to the NVPF GITT profiles in Fig. 7, the OCV voltage relaxation toward steady-state occurs faster for the HC electrode. This indicates a higher solid-state diffusivity of Na in the HC compared to the NVPF electrode.

GITT data in combination with a half-cell P2D model and optimization can be used to simultaneously determine solid-state diffusion coefficient ($D_{1,m}$) and the kinetic rate constant (k_m) as a function of the transferred charge [59,60]. The details of this optimization procedure and the P2D GITT model setup have been recently described elsewhere [33].

Fig. 9 shows the calculated diffusion coefficient ($D_{1,p}$) and rate constant for the charge transfer reaction (k_p) of the NVPF electrode. The EMF of the NVPF cathode is, for comparative reasons, also shown in (a), this allows a correlation between the EMF with the relevant parameters and various phase changes occurring in the NVPF electrode. Fig. 9b and c show $D_{1,p}$ and k_p as a func-

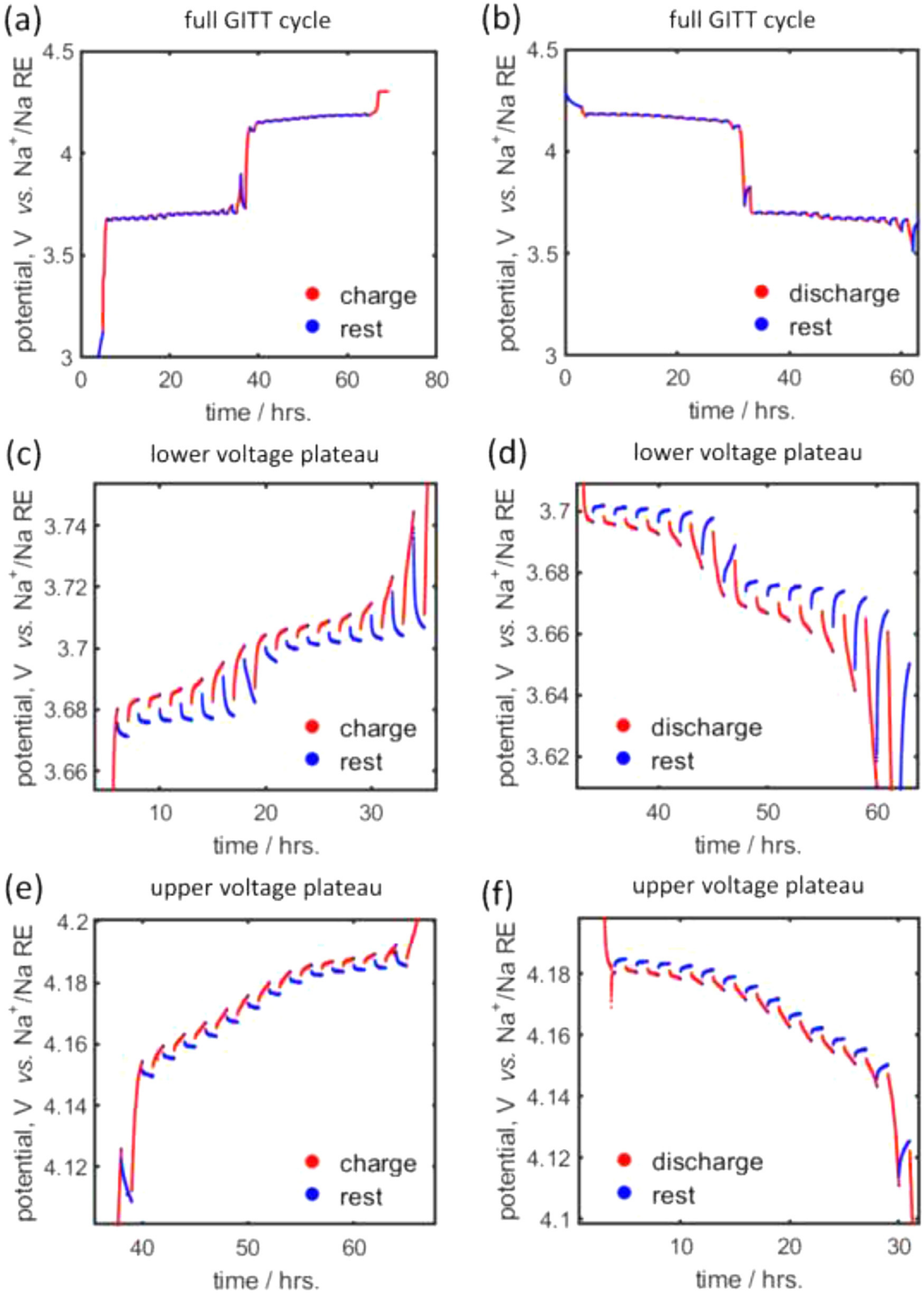

Fig. 7. GITT measurements of a Na//NVPF half-cell. Voltage profiles of 30 GITT steps obtained during charging (a) and discharging (b) in the voltage range of 3.0 to 4.3 V. Magnified view of profiles in the lower voltage plateau during charging (c) and discharging (d). Magnified view of profiles at the upper voltage plateau region during charging (e) and discharging (f).

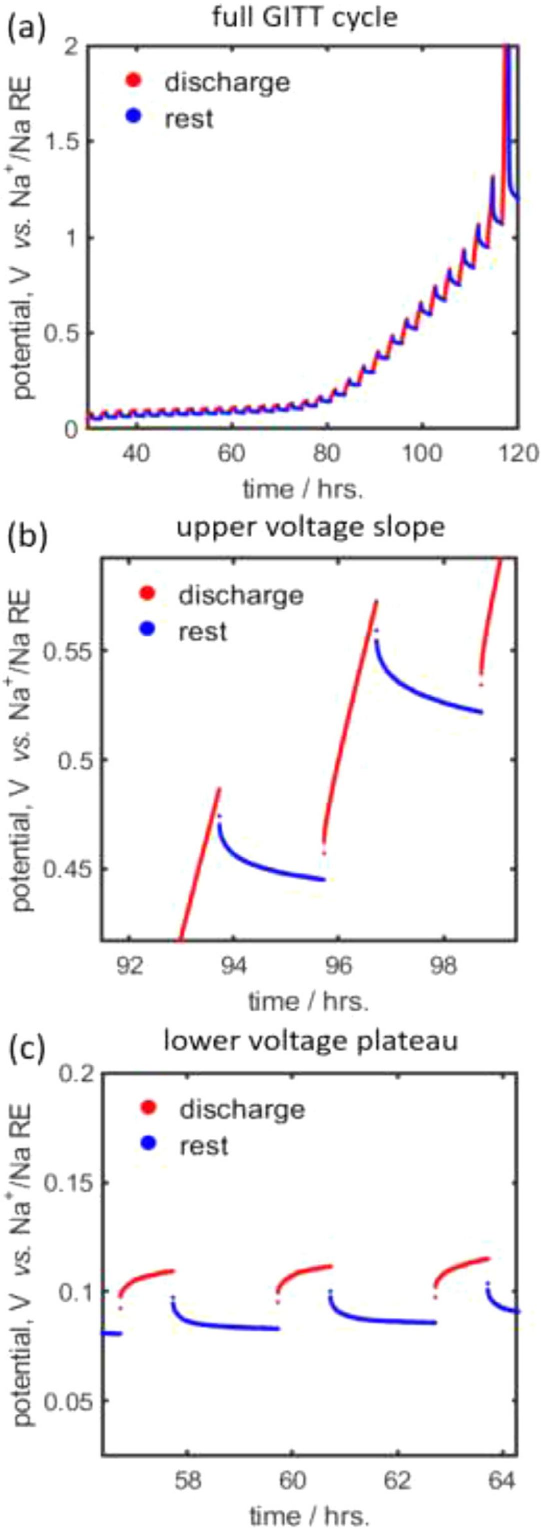

Fig. 8. GITT measurements of a Na//HC half-cell configuration. 29 discharge GITT steps are obtained in the cell voltage range 0.3 mV to 2.0 V (a). Magnified view of discharge GITT profiles obtained in the upper (b) and lower voltage region of HC (c).

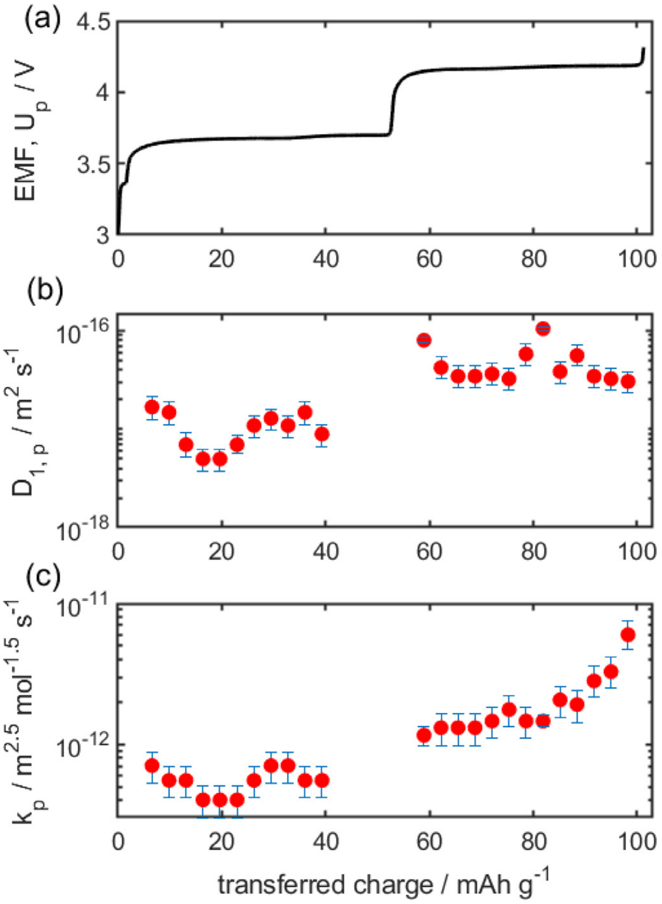

Fig. 9. NVPF parameters derived from GITT P2D simulations. EMF voltage curve of an NVPF electrode as determined by the extrapolation-to-zero-current method (a). Calculated diffusion coefficients, $D_{1,p}$ (b) and charge transfer rate constants, k_p (c) as a function of transferred charge in the electrode.

tion of transferred charge, respectively. There is a clear shift in the diffusion coefficient moving from the lower voltage plateau region (average $D_{1,p} = 1.1 \cdot 10^{-17}$ m^2 s^{-1}) to the upper voltage plateau region (average $D_{1,p} = 5.8 \cdot 10^{-17}$ m^2 s^{-1}). On the other hand, the k_p values (c) show an exponential increase as a function of the transferred charge at toward the end of the charging process. An average value of $k_p = 1.3 \cdot 10^{-12}$ m$^{2.5}$ mol$^{-1.5}$s^{-1} is obtained for all measurements. However, not all $D_{1,p}$ and k_p values could be accurately determined using the P2D GITT model, in particular at the steep voltage slope regions. This is because the single phase region is very short and it is therefore difficult to accurately define the EMF at steep voltage slope regions [33].

Fig. 10 shows results of the calculated diffusion coefficient ($D_{1,n}$) and rate constants (k_n) for the HC electrode. The EMF of HC is shown in Fig. 10a in order to align the EMF and the calculated parameters. Fig. 10b and c show $D_{1,n}$ and k_n, as function of transferred charge, respectively. Comparing NVPF and HC, two materials with different crystallographic structures and charge storage mechanisms, it is evident that the HC parameters do not exhibit a large variations as a function of transferred charge. Average values of $D_{1,n} = 3.6 \cdot 10^{-16}$ m^2 s^{-1} and $k_n = 5.5 \cdot 10^{-12}$ m$^{2.5}$ mol$^{-1.5}$s^{-1} are obtained. In addition HC parameters $D_{1,n}$ and k_n (Fig. 10b and c) are higher than NVPF parameters $D_{1,p}$ and k_p (Fig. 9b and c), This means solid-state mass transport and kinetic rates are higher in HC compared to NVPF particles.

Using the following diffusion length expression, it is now possible to estimate the time it takes for the diffusion of Na$^+$ in NVPF and HC particles. The diffusion time is calculated as

$$\tau_m = \frac{R_m^2}{4D_{1,m}}, \quad m = \{n, p\}, \tag{2}$$

where τ_m is the diffusion time in electrode particle m [s] and R_m is the mean particle radius. Taking $D_{1,p} = 1.1 \cdot 10^{-17}$ m^2 s^{-1} and $D_{1,n} = 9 \cdot 10^{-16}$ m^2 s^{-1}, the average diffusion coefficients toward

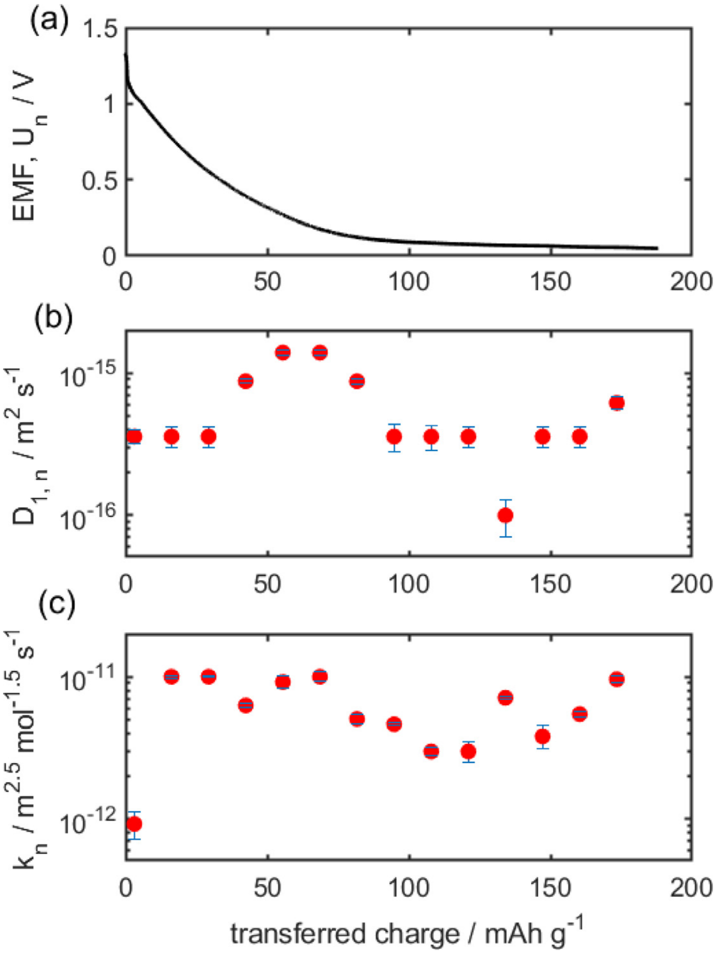

Fig. 10. HC parameters derived from GITT P2D modeling. The EMF profile of an HC electrode is determined by the extrapolation-to-zero-current method (a). Calculated diffusion coefficients, $D_{1,n}$ (b) and kinetic rate constants, k_n (c) as a function of transferred charge.

the end of discharge, the diffusion times obtained for NVPF and HC particles are $\tau_p = 2$ h and $\tau_n = 1$ hour, respectively. This shows that diffusion limitations are more severe in NVPF particles, where large concentration gradients can be expected at moderately high discharge rates above 0.5 C. That is despite the submicron mean size of the NVPF particles. The implication of these results in the P2D model setup is that the NVPF particles should have a fine mesh close to the particle surface and use concentration dependent $D_{1,p}$ and k_p parameters, in order to obtain accurate concentration profiles [61].

3.5. Complete batteries

In complete SIBs based on an NVPF cathode, a HC anode and a Na-RE, the individual electrode potentials for the NVPF (V_p) and HC (V_n) are related to the full cell voltage (V_{bat}) as

$$V_{bat} = V_p - V_n. \tag{3}$$

Fig. S4 of the Supplementary Information shows the voltage profiles obtained during the formation cycles for a HC//NVPF SIB. These profiles were obtained at a constant current of 0.2 mA (0.07C) and cutoff voltages 2 and 4.2 V. In the first formation cycle (black curves), a high capacity of 3.3 mAh is recorded. Note, the first cycle voltage profile of NVPF shown in Fig. S4b does not exhibit the same voltage artifacts as was the case in the Na//NVPF half-cells (Fig. 5a), thus confirming the effect of the Na CE to the voltage artifacts.

Fig. 11 shows the 5th (dis)charge cycle during formation. Fig. 11a shows profiles of V_{bat} while the individual voltage profiles V_p and V_n.are shown in Fig. 11b and c, respectively. It should be emphasized that the difference $V_p - V_n$ exactly matches V_{bat}. For example, at the lower cutoff voltage of 2 V, $V_p = 3.64$ V and $V_n = 1.64$ V *vs.* Na^+/Na, as expected. A characteristic feature of the HC//NVPF voltage profiles is the pronounced voltage difference between (dis)charge cycles. This was also identified in the half-cell (dis)charge profiles (Figs. 5a and 6a). Integration of the area between the (dis)charge voltage curves for V_p and V_n and comparing these two areas to the area in V_{bat} reveals that V_n accounts for 60% of the total voltage difference in full cell (dis)charge cycles. Therefore, the HC electrode has the largest contribution to the round-trip energy loss.

In terms of electrode balancing, the SIB shown in Fig. 11 is designed to maximize energy density. At full charge, the HC anode attains a high gravimetric capacity of 177 mAh g^{-1} at a low electrode potential at 0.05 V. During the same charging cycle, the NVPF cathode also attains a high reversible capacity of 89 mAh g^{-1} at 4.25 V. These gravimetric capacity calculations were based on the electrode loading of 6 mg cm^{-2} for HC and 12 mg cm^{-2} for NVPF. Nevertheless, safely charging such a high energy density SIB can be quite challenging because of the strong rate-dependent storage capacity of the HC electrode, especially in the low voltage plateau region (see Fig. 6d). This means, very low charging rates must be applied to reach full charging capacities. In practice, this will inevitably prolong the charging period of energy optimized SIBs using HC anodes.

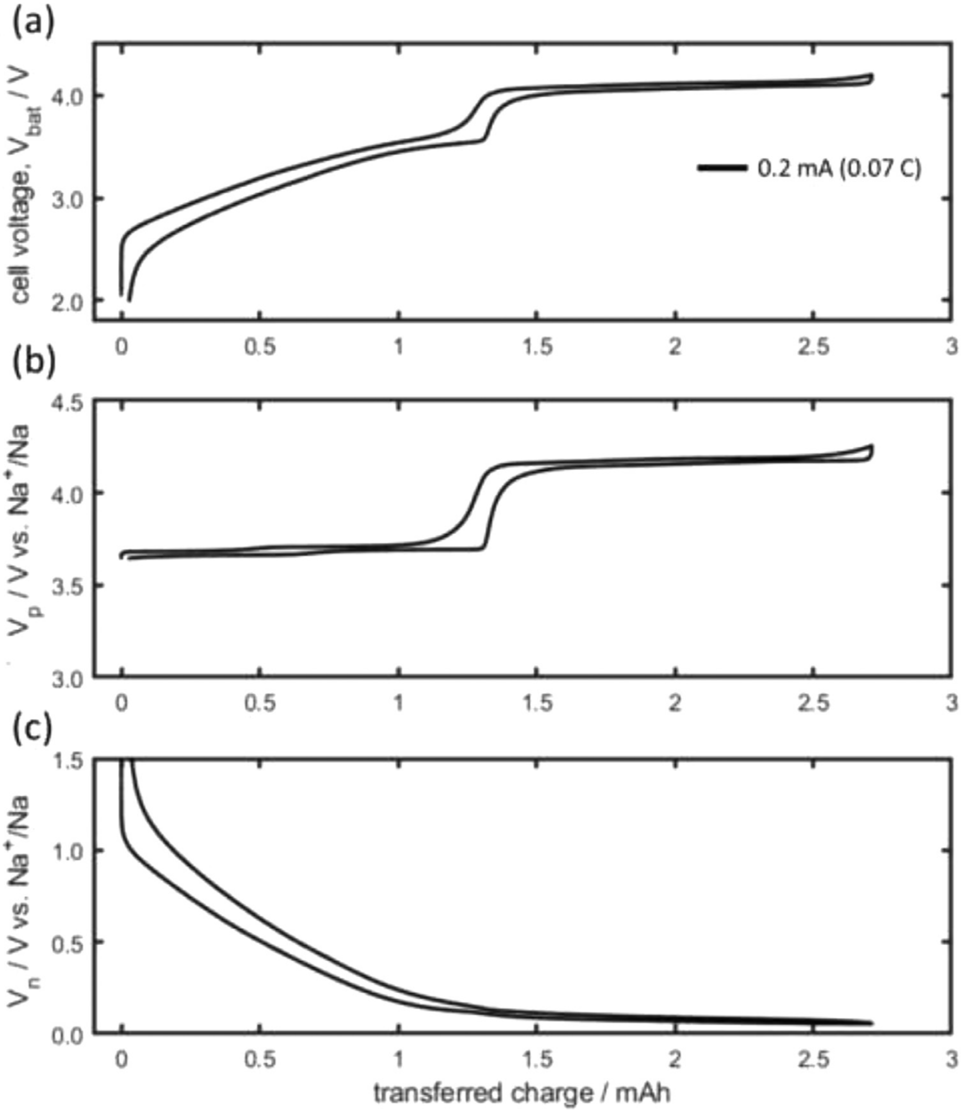

Fig. 11. Formation (dis)charge cycles of HC//NVPF full cell at 0.2 mA (0.07 C). Full cell voltage profile (a). NVPF cathode voltage profile (b). HC anode voltage profile (c). (b) and (c) measured with respect to the Na-RE.

Fig. 12 shows the voltage discharge curves of a HC//NVPF SIB at the various indicated discharge currents, in the operation range of 2 to 4.2 V. Fig. 12a shows V_{bat} measured between the NVPF and HC electrodes. Fig. 12b and c show V_p and the V_n measured *vs.* Na-RE, respectively. The capacity of the HC//NVPF full cell at 0.5 A m^{-2} (0.05 C) is 2.81 mAh (Fig. 12a). At higher discharge rates, the discharge capacity decreases due to kinetic and mass transport limitations. Increasing the discharge rate from 0.5 to 24 A m^{-2} (0.05 to 3 C), decreases the cell capacity from 2.81 to 0.94 mAh. This corresponds to a 66% decrease in storage capacity.

Another effect of increasing the discharge rate is the decrease in the cutoff electrode potentials of both V_p (b) and the V_n (c). The absolute potential change of an electrode (ΔV_m) can be calculated as

$$\Delta V_m = \left| V_m^{ini} - V_m^{cut} \right|, \quad m = \{n, p\} \tag{4}$$

where V_m^{ini} is the initial OCV of electrode *m* at full charge and V_m^{cut} is the cutoff electrode potential of electrode *m* at a given discharge rate. ΔV_m thus defines the contribution of electrode *m* to the full cell voltage drop. Therefore, the electrode with the largest ΔV_m can be viewed as the discharge capacity-limiting electrode at a given C-rate. At the slow discharge rate of 0.1 C, the negative electrode is the discharge capacity-limiting electrode because $\Delta V_p = 0.7$ V is less than $\Delta V_n = 1.5$ V. However, at 3C discharge rate, the positive electrode becomes the discharge capacity-limiting electrode, because $\Delta V_p = 1.6$ V is larger than $\Delta V_n = 0.6$ V. This means that the full cell V_{bat} profiles are dominated by the voltage change of the HC electrode at slow discharge rates, while at high discharge rates, they are dominated by the voltage change of the NVPF electrode. The high ΔV_p at high discharge rates corroborates the low diffusivity and rate constants found in the NVPF material (compare Figs. 9 and 10).

Fig. 13a shows the evaluation of individual electrode voltage drop as a function of the discharge current density. The initial voltage drop (iR) contributions from the anode and cathode are shown in Fig. 13a. The initial voltage drop is calculated as the difference between V_m^{ini} and the electrode potential soon after the discharge current pulse is applied. Linear dependencies are obtained for both electrodes, consistent with Ohm's law. The slope of these lines determines the electrode Ohmic resistance, which includes that of the current collector, the porous electrode contact resistance, the porous matrix resistance, and electrolyte resistance. The NVPF and HC electrode specific resistances are calculated to be 99.4 Ω cm^2

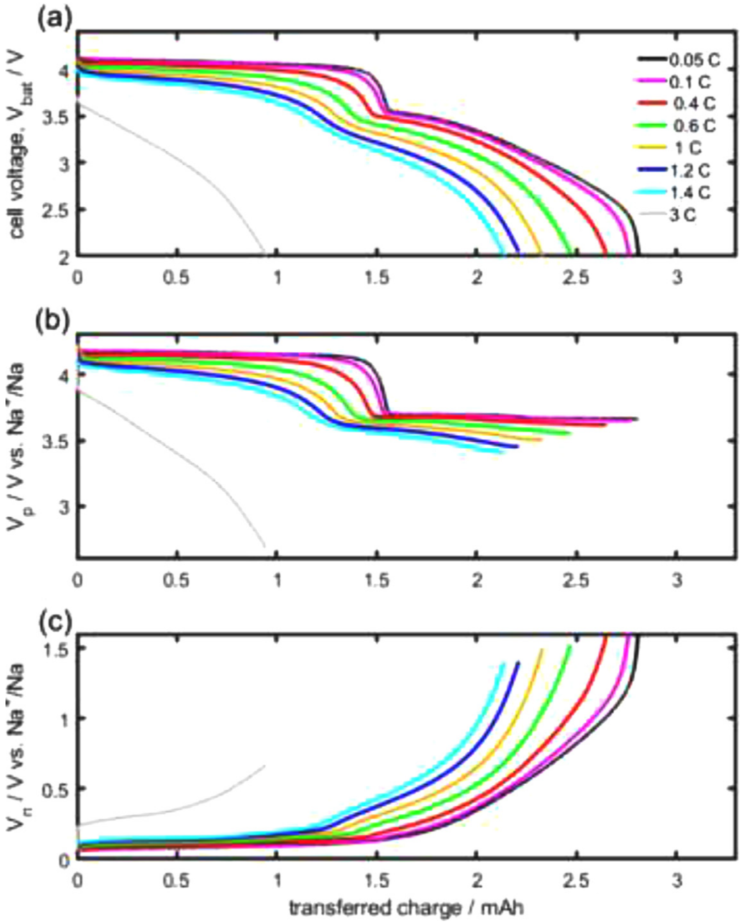

Fig. 12. HC//NVPF full cell voltage discharge profiles at different indicated C-rates (a). NVPF cathode potential during CC discharge (b). HC anode potential during CC discharge (c). (a) and (b) measured with respect to the Na-RE.

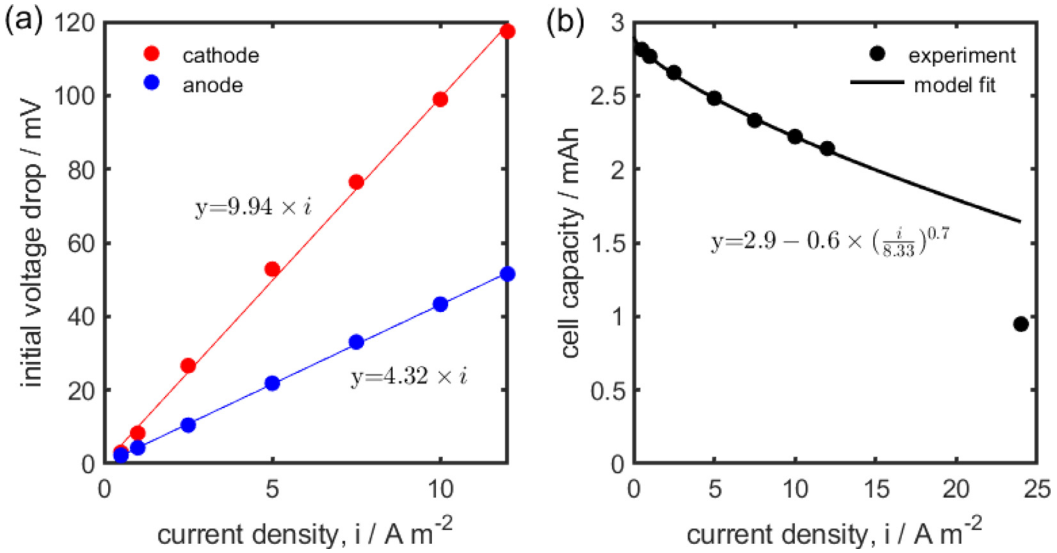

Fig. 13. Initial voltage drop contributions for the cathode (red) and anode (blue) at different discharge rates (a). Rate-dependent capacity as a function of current densities (b).

and 43.2 Ω cm^2, respectively. Therefore, improvements to the SIB cells should further seek to reduce the NVPF electrode Ohmic resistance, which is very high and more than twice that of the HC electrode. This resistance results in Joule heating in the cells, which can hinder the scalability of the cells and modules in large battery pack installations. Previous modeling reports have identified the contact resistance as the most dominant factor to the initial voltage drop [62,63]. Moreover, the NVPF material is a known poor electric conductor [64]. Therefore, there is a need to optimize the carbon conductive filler and NVPF electrode porosity. Such multiparameter optimization objectives can be guided by P2D model-based design [65].

The results in Fig. 13a may appear to contradict the low overpotentials in NVPF (shown in Fig. 5d) and the high overpotentials in HC (shown in Fig. 6d). This is because Ohmic losses only consider electronic conductivity in the solid components of the electrode. In contrast, total overpotentials additionally account for electrode kinetics and species mass transport in the electrodes and in the electrolyte [66].

Fig. 13b shows the capacity decrease of the full cell SIB as a function of the discharge current density. The capacity decreases exponentially as a function of discharge rate. Using this data, we can deduce an empirical model for the rate-dependent capacity of the SIB

$$\frac{C(i)}{C_0} = 1 - \left(1 - \frac{C(i_{1C})}{C_0}\right) \cdot \left(\frac{i}{i_{1C}}\right)^n, \tag{5}$$

where $C(i)$ is the cell capacity at discharge rate i [mAh], C_0 is the cell capacity extrapolated to zero current [mAh], i_{1C} is the 1-hour discharge current [A m^{-2}] and n is the dimensionless exponent. For this SIB, $C_0 = 2.9$ mAh, $C(i_{1C}) = 2.3$ mAh, $i_{1C} = 8.33$ A m^{-2} and $n = 0.7$. Eq. (5) is analogous to Peukert's law [67,68] and can be applied to deduce $C(i)$ for a constant discharge rate, and benchmark the rate performances of different SIBs. The only unknowns are C_0 and n which can be found by optimization. Alternatively, C_0 can be taken from the EMF. A further simplification is that Eq. (5) is dimensionless and therefore can be applied to any SIB cell of a different dimension. Nevertheless, this relationship is not applicable at the very high discharge rates.

Using the maximum cell capacity of 2.9 mAh and electrode loading of 12 and 6 mg cm^{-2} for NVPF and HC, respectively, it is now possible to determine Q_m^{rev} the maximum reversible capacities of both electrodes. Q_p^{rev} =95 mAh g^{-1} and Q_n^{rev} =190 mAh g^{-1} for NVPF and HC electrodes, respectively. These values are close to the EMF capacities of 101 mAh g^{-1} (Fig. 5c) and 222 (Fig. 6c) obtained in Na//NVPF and Na//HC half-cells, respectively. The half-cell and full cell values therefore only differ slightly.

For modeling purposes, it is also convenient to determine the maximum and minimum reversible concentrations in the particles. This definition can be given as

$$c_{1,m}^{max} = 3.6 \frac{\rho_m \, Q_m^{\max}}{F}, \quad m = \{n, p\} \tag{6}$$

$$c_{1,m}^{min} = 3.6 \frac{\rho_m \, Q_m^{\min}}{F}, \quad m = \{n, p\} \tag{7}$$

where $c_{1,m}^{max}$ and $c_{1,m}^{min}$ are the maximum and minimum concentrations in the electrode particles, respectively [mol m^{-3}], ρ_m is the active material density [g m^{-3}], $Q_m^{\max}$ the maximum gravimetric capacity in the electrode [mAh g^{-1}], $Q_m^{\min}$ the non-extractable charge [mAh g^{-1}], and F is the Faraday constant 96,485 [C mol^{-1}]. The factor 3.6 originates from the conversion of charge units from coulomb to mAh. Based on Eq. (1), $Q_p{}^{\max} =$ 128 mAh g^{-1}, while $Q_n{}^{\max} =$ 222 mAh g^{-1} is based on the EMF since there is no general equation for charge insertion in HC .

In addition, the maximum stoichiometric index, $s_m^{max} = 1$ and the minimum stoichiometric index, s_m^{min} can be defined using the equation

$$s_m^{min} = \frac{c_{1,m}^{min}}{c_{1,m}^{max}}, \; m = \{n, p\} \tag{8}$$

Table 2 summarizes the electrode parameters deduced from the above electrochemical tests.

Another figure of merit to benchmark the performance of the HC//NVPF complete SIB is the Ragone plot, a logarithmic plot of energy density *vs.* power density and herein shown in Fig. 14. The energy density is calculated based on the total mass loading of the active materials (*i.e.* 6 mg cm^{-2} HC and 12 mg cm^{-2} NVPF). Although high power operations such as discharge in less than 12 min are possible, there is a significant loss of energy density at these rates. Considering the results in Fig. 9b and Fig. 13a, the discharge power density of the HC//NVPF SIB is limited by the performance of NVPF at high rates due to the material's low solid-state diffusivity and high Ohmic drop. While low discharge rates, such as discharge in 5 h (0.2 C), maximize the energy density and efficiency of the SIB, such operations, however, come at the inconvenience of low power density. The optimum compromise between energy and power density is therefore found at the "knee" of the Ragone plot, which corresponds to approximately the 1 C-rate (8.33 A m^{-2}) for the investigated electrode configuration.

4. Conclusions

This work presented experimental methods and results of sodium-ion battery (SIB) electrode materials based on hard carbon (HC) anode and $Na_3V_2(PO_4)_2F_3$ (NVPF) cathode. These experiments were conducted in half-cell and full cell setups, wherein a Na reference electrode (Na-RE) was used as a third electrode. As a result, the geometric, thermodynamic, and kinetic parameters necessary for physics-based SIB modeling, were deduced.

Based on the analysis of physical properties, the electrodes particles generally exhibit irregular shapes and a wide particle size distribution. This is most evident in the HC particles. The knowledge of the particle sizes allowed the determination of the diffusion coefficients and the kinetic rate constants as a function of the transferred charge. The results show that HC's diffusion coefficient is an order of magnitude higher than that of NVPF. As a result, improving the high rate performance of the SIB is a question of overcoming diffusion mass transport limitations.

In the analysis of the full cell, the HC electrode shows impressively low Ohmic resistance, and high discharge rate capability. However, the HC anode contributes 60% of the total voltage differences between (dis)charge cycles at low rates. Moreover, accessing the maximum capacity of the HC electrodes using constant current charging proved a challenge, even at very low currents. This drawback could hinder the fast charging operations of HC-based SIBs. Battery management will undoubtedly require smart algorithms to attain the maximum capacity safely.

On the cathode side, the NVPF electrode exhibits outstanding performance in terms of low overpotentials and capacity retention at low rates. However, the NVPF electrode exhibits more than twice the Ohmic resistance of the HC electrode. Further, it becomes the limiting electrode at high discharge rates. The poor rate performance is related to the low diffusion coefficient in the material. The high Ohmic resistance is mainly attributed to the low NVPF conductivity. This Ohmic resistance can also result in Joule heating challenges in battery thermal management when the cells are scaled up. Therefore, NVPF electrode improvement should focus on optimizing the particle sizes, and carbon conductive additive. Other strategies include carbon-coating on the NVPF particles as well as the Al current collectors.

Overall, the performances of the HC//NVPF SIBs are promising, and the results herein demonstrate chemistry and technology with real prospects for scale-up. This conclusion can be drawn because the issues outlined above can be addressed through electrode design improvements. SIBs can thus be expected to drop-in replace incumbent technologies in myriad battery energy storage applications, in particular the stationary applications of peak shaving, time-shifting, and congestion relief. This complementary feature of SIBs will further alleviate Li supply shortage risk and result in

Table 2
SIB parameters concluded from the electrochemical investigations.

Parameter	Unit	Description	NVPF electrode	HC electrode	Cell
C_{cell}	mAh	Cell capacity$^{(a)}$	-	-	2.9
M_m	mg cm^{-2}	Active mass loading	12	6	-
Q_m^{rev}	mAh g^{-1}	Reversible capacity$^{(b)}$	95	190	-
Q_m^{max}	mAh g^{-1}	Maximum capacity$^{(c)}$	128	222	-
Q_m^{min}	mAh g^{-1}	Non-extractable charge $^{(d)}$	33	32	-
$c_{1,m}^{max}$	mol l^{-1}	Maximum concentration	15.3	16.2	-
$c_{1,m}^{min}$	mol l^{-1}	Minimum concentration	3.9	2.3	-
s_m^{max}	–	Maximum stoichiometric index	1	1	-
s_m^{min}	–	Minimum stoichiometric index	0.25	0.14	-
$R_{contact,m}$	Ω cm^2	Contact resistance	99.4	43.2	142.6

(a) based on extrapolation to zero current of the HC//NVPF SIB reversible capacity
(b) reversible electrode capacity from full cell measurements, $Q_m^{rev} = C_{cell}/(M_m \cdot A)$
(c) based on the theoretical capacity of NVPF and EMF capacity of HC
(d) $Q_m^{min} = Q_m^{max} - Q_m^{rev}$

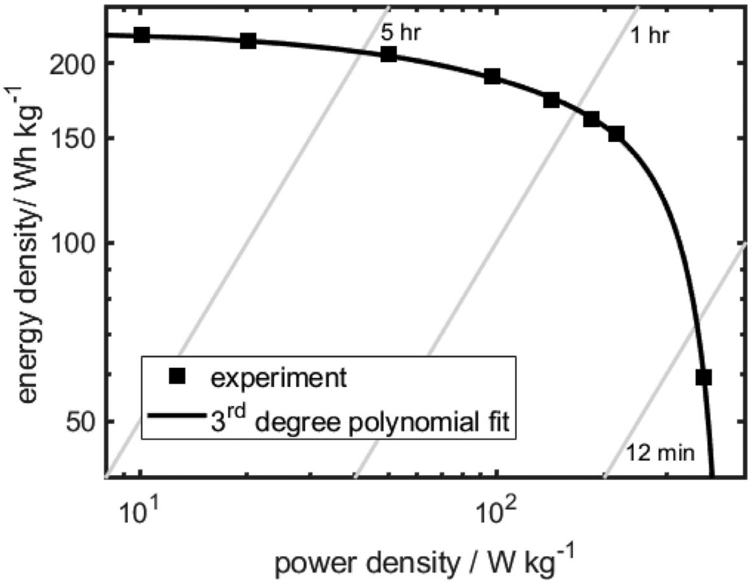

Fig. 14. Experimentally obtained Ragone plot for an HC//NVPF SIB.

increased integration of intermittent energy sources in electricity grids.

Declaration of Competing Interest

The authors declare no conflict of interest.

Acknowledgements

D.L.D. has received funding from the European Union's Horizon 2020 Research and Innovation Program under Grant Agreement no. 769900-DEMOBASE. K.C. and G.M. are grateful for the support from the European Union's Horizon 2020 Research and Innovation Program under Grant Agreement no. 646433-NAIADES. KC highly appreciates support from the Living Lab Energy Campus (LLEC) at the Forschungszentrum Jülich.

Kudakwashe Chayambuka: Investigation, Writing - Original Draft. Ming Jiang: Investigation. Grietus Mulder: Supervision, Writing - Review and Editing. Dmitri L. Danilov: Supervision, Writing - Review and Editing. Peter H. L. Notten: Resources, Supervision, Writing - Review and Editing.

Declaration of Competing Interest

The authors declare that they have no conflict interests.

Supplementary materials

Supplementary material associated with this article can be found, in the online version, at doi:10.1016/j.electacta.2021.139726.

References

[1] K. Chayambuka, G. Mulder, D.L. Danilov, P.H.L. Notten, From Li-ion batteries toward Na-ion chemistries: challenges and opportunities, Adv. Energy Mater. 10 (2020) 2001310 https://doi.org/10.1002/aenm.202001310.
[2] K. Chayambuka, G. Mulder, D.L. Danilov, P.H.L. Notten, Sodium-ion battery materials and electrochemical properties reviewed, Adv. Energy Mater. 8 (2018) 1800079 https://doi.org/10.1002/aenm.201800079.
[3] A. Eftekhari, D.-W. Kim, Sodium-ion batteries: new opportunities beyond energy storage by lithium, J. Power Source. 395 (2018) 336–348 https://doi.org/10.1016/j.jpowsour.2018.05.089.
[4] P. Ge, M. Fouletier, Electrochemical intercalation of sodium in graphite, Solid State Ion. 28 (1988) 1172–1175 https://doi.org/10.1016/0167-2738(88)90351-7.
[5] D.A. Stevens, J.R. Dahn, High capacity anode materials for rechargeable sodium-ion batteries, J. Electrochem. Soc. 147 (2000) 1271–1273 https://doi.org/10.1149/1.1393348.
[6] D.A. Stevens, J.R. Dahn, The mechanisms of lithium and sodium insertion in carbon materials, J. Electrochem. Soc. 148 (2001) A803–A811 https://doi.org/10.1149/1.1379565.
[7] D. Larcher, J.-M. Tarascon, Towards greener and more sustainable batteries for electrical energy storage, Nat. Chem. 7 (2015) 19–29 https://doi.org/10.1038/nchem.2085.
[8] TiamatPowerful, Fast charging, Enduring Cells Thanks to Sodium-Ion, 2020 http://www.tiamat-energy.com/(accessed April 14, 2020).

[9] A. Bauer, J. Song, S. Vail, W. Pan, J. Barker, Y. Lu, The scale-up and commercialization of nonaqueous Na-ion battery technologies, Adv. Energy Mater. 8 (2018) 1702869 https://doi.org/10.1002/aenm.201702869.

[10] J. Ayre, 18650 *Sodium-Ion Battery Developed At RS2E, CleanTechnica*, 2015 https://cleantechnica.com/2015/12/01/18650-sodium-ion-battery-developed-at-rs2e/(accessed April 14, 2020).

[11] FaradionSodium-ion Technology, Faradion Limited, 2021 (n.d.).

[12] J. Barker, Commercialization of Faradion's High Energy Density Na-ion Battery Technology, 2016.

[13] T. Broux, F. Fauth, N. Hall, Y. Chatillon, M. Bianchini, T. Bamine, J.-B. Leriche, E. Suard, D. Carlier, Y. Reynier, L. Simonin, C. Masquelier, L. Croguennec, High rate performance for carbon-coated Na3V2(PO4)2F3 in Na-ion batteries, Small Method. 3 (2019) 1800215 https://doi.org/10.1002/smtd.201800215.

[14] Y.-S. Hu, S. Komaba, M. Forsyth, C. Johnson, T. Rojo, A new emerging technology: Na-ion batteries, Small Method. 3 (2019) 1900184 https://doi.org/10.1002/smtd.201900184.

[15] Altris - We enable the Next Generation of Batteries, 2021 (n.d.). https://www.altris.se/(accessed April 8, 2021).

[16] A. Ponrouch, E. Marchante, M. Courty, J.-.M. Tarascon, M.Rosa Palacín, In search of an optimized electrolyte for Na-ion batteries, Energy Environ. Sci. 5 (2012) 8572–8583 https://doi.org/10.1039/C2EE22258B.

[17] J. Barker, M.Y. Saidi, J.L. Swoyer, A sodium-ion cell based on the fluorophosphate compound NaVPO4 F, Electrochem. Solid-State Lett. 6 (2003) A1–A4.

[18] M. Bianchini, N. Brisset, F. Fauth, F. Weill, E. Elkaim, E. Suard, C. Masquelier, L. Croguennec, Na3V2(PO4)2F3 revisited: a high-resolution diffraction study, Chem. Mater. 26 (2014) 4238–4247 https://doi.org/10.1021/cm501644g.

[19] M. Bianchini, F. Fauth, N. Brisset, F. Weill, E. Suard, C. Masquelier, L. Croguennec, Comprehensive investigation of the Na3V2(PO4)2F3–NaV2(PO4)2F3 system by operando high resolution synchrotron X-ray diffraction, Chem. Mater. 27 (2015) 3009–3020 https://doi.org/10.1021/acs.chemmater.5b00361.

[20] R.K.B. Gover, A. Bryan, P. Burns, J. Barker, The electrochemical insertion properties of sodium vanadium fluorophosphate, Na3V2(PO4)2F3, Solid State Ion. 177 (2006) 1495–1500 https://doi.org/10.1016/j.ssi.2006.07.028.

[21] J. Barker, R.K.B. Gover, P. Burns, A.J. Bryan, Hybrid-ion A lithium-ion cell based on a sodium insertion material, Electrochem. Solid-State Lett. 9 (2006) A190–A192 https://doi.org/10.1149/1.2168288.

[22] N. Eshraghi, S. Caes, A. Mahmoud, R. Cloots, B. Vertruyen, F. Boschini, Sodium vanadium (III) fluorophosphate/carbon nanotubes composite (NVPF/CNT) prepared by spray-drying: good electrochemical performance thanks to well-dispersed CNT network within NVPF particles, Electrochim. Acta 228 (2017) 319–324 https://doi.org/10.1016/j.electacta.2017.01.026.

[23] R.A. Shakoor, D.-H. Seo, H. Kim, Y.-U. Park, J. Kim, S.-W. Kim, H. Gwon, S. Lee, K. Kang, A combined first principles and experimental study on Na 3 V 2 (PO 4) 2 F 3 for rechargeable Na batteries, J. Mater. Chem. 22 (2012) 20535–20541 https://doi.org/10.1039/C2JM33862A.

[24] P. Serras, V. Palomares, A. Goñi, P. Kubiak, T. Rojo, Electrochemical performance of mixed valence Na3V2O2x(PO4)2F3−2x/C as cathode for sodium-ion batteries, J. Power Source. 241 (2013) 56–60 https://doi.org/10.1016/j.jpowsour.2013.04.094.

[25] S. Qiu, L. Xiao, M.L. Sushko, K.S. Han, Y. Shao, M. Yan, X. Liang, L. Mai, J. Feng, Y. Cao, X. Ai, H. Yang, J. Liu, Manipulating adsorption–insertion mechanisms in nanostructured carbon materials for high-efficiency sodium ion storage, Adv. Energy Mater. 7 (2017) n/a-n/ahttps://doi.org/10.1002/aenm.201700403.

[26] P. Tsai, S.-C. Chung, S. Lin, A. Yamada, Ab initio study of sodium intercalation into disordered carbon, J. Mater. Chem. A 3 (2015) 9763–9768 https://doi.org/10.1039/C5TA01443C.

[27] C. Bommier, T.W. Surta, M. Dolgos, X. Ji, New mechanistic insights on Na-ion storage in nongraphitizable carbon, Nano Lett. 15 (2015) 5888–5892 https://doi.org/10.1021/acs.nanolett.5b01969.

[28] B. Zhang, C.M. Ghimbeu, C. Laberty, C. Vix-Guterl, J.-M. Tarascon, Correlation between microstructure and Na storage behavior in hard carbon, Adv. Energy Mater. 6 (2016) n/a-n/ahttps://doi.org/10.1002/aenm.201501588.

[29] K. Chayambuka, G. Mulder, D.L. Danilov, P.H.L. Notten, Physics-based modeling of sodium-ion batteries part II. model and validation, Electrochim. Acta (2021), https://doi.org/10.1016/j.electacta.2021.139764.

[30] N. Jin, D.L. Danilov, P.M.J.V. den Hof, M.C.F. Donkers, Parameter estimation of an electrochemistry-based lithium-ion battery model using a two-step procedure and a parameter sensitivity analysis, Int. J. Energy Res. 42 (2018) 2417–2430 https://doi.org/10.1002/er.4022.

[31] C.M. Doyle, Design and Simulation of Lithium Rechargeable Batteries, Lawrence Berkeley National Laboratory., 1995 http://escholarship.org/uc/item/6j87z0sp (accessed April 11, 2017).

[32] C.-H. Chen, F.B. Planella, K. O'Regan, D. Gastol, W.D. Widanage, E. Kendrick, Development of experimental techniques for parameterization of multi-scale lithium-ion battery models, J. Electrochem. Soc. 167 (2020) 080534 https://doi.org/10.1149/1945-7111/ab9050.

[33] K. Chayambuka, G. Mulder, D.L. Danilov, P.H.L. Notten, Determination of state-of-charge dependent diffusion coefficients and kinetic rate constants of phase changing electrode materials using physics-based models, J. Power Source. Adv. 9 (2021) 100056 https://doi.org/10.1016/j.powera.2021.100056.

[34] EU H2020 ProgramNaiades, Sodium ion batteries, 2020 http://www.naiades.eu/(accessed August 29, 2017).

[35] NaiadesSodium Ion Batteries, 2021 (n.d.)https://www.naiades.eu/(accessed April 15, 2020).

[36] R. Dugas, J.D. Forero-Saboya, A. Ponrouch, Methods and protocols for reliable electrochemical testing in post-Li batteries (Na, K, Mg, and Ca), Chem. Mater. 31 (2019) 8613–8628 https://doi.org/10.1021/acs.chemmater.9b02776.

[37] J. Conder, C. Villevieille, How reliable is the Na metal as a counter electrode in Na-ion half cells? Chem. Commun. 55 (2019) 1275–1278 https://doi.org/10.1039/C8CC07852A.

[38] D.I. Iermakova, R. Dugas, M.R. Palacín, A. Ponrouch, On the comparative stability of Li and Na metal anode interfaces in conventional alkyl carbonate electrolytes, J. Electrochem. Soc. 162 (2015) A7060 https://doi.org/10.1149/2.0091513jes.

[39] New Separator For PAT Insulation Sleeves | EL-CELL, 2021 (n.d.). https://el-cell.com/new-separator-for-pat-insulation-sleeves/(accessed March 5, 2021).

[40] R. Dugas, B. Zhang, P. Rozier, J.M. Tarascon, Optimization of Na-Ion battery systems based on polyanionic or layered positive electrodes and carbon anodes, J. Electrochem. Soc. 163 (2016) A867–A874 https://doi.org/10.1149/2.0051605jes.

[41] X. Chen, Y. Zheng, W. Liu, C. Zhang, S. Li, J. Li, High-performance sodium-ion batteries with a hard carbon anode: transition from the half-cell to full-cell perspective, Nanoscale 11 (2019) 22196–22205 https://doi.org/10.1039/C9NR07545C.

[42] W.H. Smyrl, J. Newman, Current distribution at electrode edges at high current densities, J. Electrochem. Soc. 136 (1989) 132 https://doi.org/10.1149/1.2096572.

[43] A. Verma, K. Smith, S. Santhanagopalan, D. Abraham, K.P. Yao, P.P. Mukherjee, Galvanostatic intermittent titration and performance based analysis of LiNi0.5Co0.2Mn0.3O2 cathode, J. Electrochem. Soc. 164 (2017) A3380 https://doi.org/10.1149/2.1701713jes.

[44] C.-J. Bae, C.K. Erdonmez, J.W. Halloran, Y.-M. Chiang, Design of battery electrodes with dual-scale porosity to minimize tortuosity and maximize performance, Adv. Mater. 25 (2013) 1254–1258 https://doi.org/10.1002/adma.201204055.

[45] The Impact of Particle Size and Shape On Battery Electrode Slurry Formation | Malvern Panalytical, 2021 (n.d.). https://www.malvernpanalytical.com/en/learn/knowledge-center/application-notes/AN170103BatterySlurryParticleSize-Shape (accessed March 9, 2021).

[46] J. Maurath, B. Bitsch, Y. Schwegler, N. Willenbacher, Influence of particle shape on the rheological behavior of three-phase non-brownian suspensions, Colloids Surf. A 497 (2016) 316–326 https://doi.org/10.1016/j.colsurfa.2016.03.006.

[47] Y. Sumiyama, N. Sakai, (Sumitomo Bakelite Co.), JP2016136452 (A), 2016 https://worldwide.espacenet.com/publicationDetails/biblio?FT=D&date=20160728&DB=EPODOC&locale=en_EP&CC=JP&NR=2016136452A&KC=A&ND=4 (accessed March 5, 2018).

[48] E. Berg, C. Villevieille, D. Streich, S. Trabesinger, P. Novak, Rechargeable batteries: grasping for the limits of chemistry, J. Electrochem. Soc. 162 (2015) A2468–A2475.

[49] G. Hasegawa, K. Kanamori, N. Kannari, J. Ozaki, K. Nakanishi, T. Abe, Hard carbon anodes for Na-ion batteries: toward a practical use, ChemElectroChem 2 (2015) 1917–1920 https://doi.org/10.1002/celc.201500412.

[50] K.-H. Chen, V. Goel, M.J. Namkoong, M. Wied, S. Müller, V. Wood, J. Sakamoto, K. Thornton, N.P. Dasgupta, Enabling 6C fast charging of Li-ion batteries with graphite/hard carbon hybrid anodes, Adv. Energy Mater. 11 (2021) 2003336 https://doi.org/10.1002/aenm.202003336.

[51] C.F. Armer, M. Lübke, M.V. Reddy, J.A. Darr, X. Li, A. Lowe, Phase change effect on the structural and electrochemical behaviour of pure and doped vanadium pentoxide as positive electrodes for lithium ion batteries, J. Power Source. 353 (2017) 40–50 https://doi.org/10.1016/j.jpowsour.2017.03.121.

[52] C. Delmas, H. Cognac-Auradou, J. Cocciantelli, M. Menetrier, J. Doumerc, The LixV2O5 system: an overview of the structure modifications induced by the lithium intercalation, Solid State Ion. 69 (1994) 257–264 https://doi.org/10.1016/0167-2738(94)90414-6.

[53] N. Kazemi, D.L. Danilov, L. Haverkate, N.J. Dudney, S. Unnikrishnan, P.H.L. Notten, Modeling of all-solid-state thin-film Li-ion batteries: accuracy improvement, Solid State Ion. 334 (2019) 111–116 https://doi.org/10.1016/j.ssi.2019.02.003.

[54] D. Danilov, R.a.H. Niessen, P.H.L. Notten, modeling all-solid-state Li-ion batteries, J. Electrochem. Soc. 158 (2011) A215–A222 https://doi.org/10.1149/1.3521414.

[55] D. Li, D.L. Danilov, L. Gao, Y. Yang, P.H.L. Notten, Degradation mechanisms of C6/LiFePO4 batteries: experimental analyses of cycling-induced aging, Electrochim. Acta 210 (2016) 445–455 https://doi.org/10.1016/j.electacta.2016.05.091.

[56] E. Irisarri, A. Ponrouch, M.R. Palacin, Review—hard carbon negative electrode materials for sodium-ion batteries, J. Electrochem. Soc. 162 (2015) A2476–A2482 https://doi.org/10.1149/2.0091514jes.

[57] A. Ledovskikh, D. Danilov, P.H.L. Notten, Modeling of hydrogen storage in hydride-forming materials: equilibrium gas-phase kinetics, Phys. Rev. B. 76 (2007) 064106 https://doi.org/10.1103/PhysRevB.76.064106.

[58] R.B. Smith, E. Khoo, M.Z. Bazant, Intercalation kinetics in multiphase-layered materials, J. Phys. Chem. C. 121 (2017) 12505–12523 https://doi.org/10.1021/acs.jpcc.7b00185.

[59] J. Li, F. Yang, X. Xiao, M.W. Verbrugge, Y.-T. Cheng, Potentiostatic intermittent titration technique (PITT) for spherical particles with finite interfacial kinetics, Electrochim. Acta 75 (2012) 56–61 https://doi.org/10.1016/j.electacta.2012.04.050.

[60] A. Hess, Q. Roode-Gutzmer, C. Heubner, M. Schneider, A. Michaelis, M. Bobeth, G. Cuniberti, Determination of state of charge-dependent asymmetric Butler–Volmer kinetics for LixCoO2 electrode using GITT measurements, J. Power Source. 299 (2015) 156–161 https://doi.org/10.1016/j.jpowsour.2015.07.080.

[61] K. Chayambuka, G. Mulder, D.L. Danilov, P.H.L. Notten, A hybrid backward euler control volume method to solve the concentration-dependent solid-state diffusion problem in battery modeling, J. Appl. Math. Phys. 8 (2020) 1066–1080 https://doi.org/10.4236/jamp.2020.86083.

[62] M. Doyle, J. Newman, A.S. Gozdz, C.N. Schmutz, J.-.M. Tarascon, Comparison of modeling predictions with experimental data from plastic lithium ion cells, J. Electrochem. Soc. 143 (1996) 1890–1903 https://doi.org/10.1149/1.1836921.

[63] D.E. Stephenson, E.M. Hartman, J.N. Harb, D.R. Wheeler, Modeling of particle-particle interactions in porous cathodes for lithium-ion batteries, J. Electrochem. Soc. 154 (2007) A1146–A1155.

[64] F. Sauvage, E. Quarez, J.-.M. Tarascon, E. Baudrin, Crystal structure and electrochemical properties *vs.* Na+ of the sodium fluorophosphate Na1.5VOPO4F0.5, Solid State Sci. 8 (2006) 1215–1221 https://doi.org/10.1016/j.solidstatesciences.2006.05.009.

[65] S.F. Schneider, C. Bauer, P. Novák, E.J. Berg, A modeling framework to assess specific energy, costs and environmental impacts of Li-ion and Na-ion batteries, Sustain. Energy Fuels 3 (2019) 3061–3070 https://doi.org/10.1039/C9SE00427K.

[66] W. Wang, X. Wei, D. Choi, X. Lu, G. Yang, C. Sun, Chapter 1 - Electrochemical cells for medium- and large-scale energy storage: fundamentals, in: C. Menictas, M. Skyllas-Kazacos, T.M. Lim (Eds.), Advances in Batteries for Medium and Large-Scale Energy Storage, Woodhead Publishing, 2015, pp. 3–28. https://doi.org/10.1016/B978-1-78242-013-2.00001-7.

[67] D. Doerffel, S.A. Sharkh, A critical review of using the Peukert equation for determining the remaining capacity of lead-acid and lithium-ion batteries, J. Power Source. 155 (2006) 395–400 https://doi.org/10.1016/j.jpowsour.2005.04.030.

[68] G. Mulder, N. Omar, S. Pauwels, M. Meeus, F. Leemans, B. Verbrugge, W. De Nijs, P. Van den Bossche, D. Six, J. Van Mierlo, Comparison of commercial battery cells in relation to material properties, Electrochim. Acta 87 (2013) 473–488 https://doi.org/10.1016/j.electacta.2012.09.042.